Next Materials 12 (2026) 102081

Contents lists available at ScienceDirect

Next Materials

journal homepage: www.sciencedirect.com/journal/next-materials

Research article

Integrated DFT and SCAPS-1D analysis of Tl_2AgAsX_6 (X = Cl, I) double perovskites for advanced energy-harvesting devices

R.M. Tanvir [a,b], Md. Al-Amin [a,b], S. Sheikh [a,b], A. Rayhan [c], S. Mahmud [a,b,*]

[a] Smart Computing Research Laboratory (SCRL), Department of EEE, Jatiya Kabi Kazi Nazrul Islam University, Mymensingh 2224, Bangladesh
[b] Department of EEE, Jatiya Kabi Kazi Nazrul Islam University, Mymensingh 2224, Bangladesh
[c] Department of Arts and Science, Bangladesh Army University of Science and Technology (BAUST), Sayadpur, Bangladesh

ARTICLE INFO

Keywords:
DFT
Stability
Indirect band gap
Photovoltaic efficiency
Figure of merit

ABSTRACT

Utilizing density functional theory (DFT), this research explores the stability, opto-electronic, photovoltaic, and thermoelectric potential of double perovskites Tl_2AgAsX_6 (X = Cl, I) as material candidates for energy harvesting functions. Tolerance and octahedral factor analysis reveal the cubic lattice structural stability, and the formation energies are negative, confirming their dynamic stability. Mechanical properties like Pugh's ratio, Poisson's ratio, and Cauchy pressure indicate the consistency of ductility behavior and support the good thermomechanical performance. Other relevant electronic properties obtained from application of the TB-mBJ method show indirect band gaps of 1.692 eV for $Tl_2AgAsCl_6$ and 0.882 eV for $Tl_2AgAsCl_6$. We analyze its optical properties and find high absorption coefficients in the visible range of 10^4 to 10^5 order, which are ideal for photovoltaic applications. As a result, we found the maximum efficiency of 23.38% and 16.76% for the titled materials. We have characterized the thermoelectric transport properties to obtain figures of merit (ZT) for $Tl_2AgAsCl_6$ and Tl_2AgAsI_6 at 300 K, which are 0.28 and 0.40, respectively. The favorable opto-electronic and thermoelectric properties promote these materials as promising candidates for sustainable energy technologies, such as solar cells and thermoelectric devices.

1. Introduction

Global economic growth and human welfare improvement are inextricably linked to access to energy, and the demand for it remains high due to technological advancements. However, the global energy infrastructure still relies heavily on fossil fuels, which are both limited resources and environmentally hazardous [1,2]. In response, significant research has been directed toward sustainable and renewable energy sources to ensure a stable and cleaner future [3–5]. Solar energy appears to be one of the most promising alternatives, with great potential due to its abundance. The relatively recent development of perovskite solar cells in the field of photovoltaics has brought forward a promising combination of high-power conversion efficiency, low production cost, and ease of fabrication as the primary benefits of these devices [6,7]. Overall, the key advantages of perovskite materials in solar cells are their intrinsically high light absorption and excellent charge transport properties [8]. Unfortunately, these solar cells have been hindered by multiple challenges, mainly due to the toxicity of lead and their relatively short lifetime and limited long-term stability. However, these lead-free variants currently suffer from lower efficiencies due to inherent material limitations.

Sustainable energy conversion currently relies heavily on photovoltaic and thermoelectric systems, which generate electrical power from solar radiation and recover industrial waste heat. The performance of these technologies is fundamentally governed by the materials used. In the case of the double perovskites, one of the significant characteristics is the involvement of the M-site cationic configuration, such as the one with a formal 4^+ charge state, which exceeds the 2^+ upper limit of single-perovskite structures [9]. The performance of these technologies reinforces the nature of the materials involved. In Crystallography, this results in a three-dimensional network of corner-sharing $[M'X_6]$ and $[M''X_6]$ octahedra, with A-site cations occupying the interstitial spaces [10]. While lead-based double perovskites have demonstrated remarkable power conversion efficiencies exceeding 20% [11,12], concerns about their toxicity and overall material instability have sparked interest in safer alternatives, spurring the development of lead-free double

* Corresponding author at: Smart Computing Research Laboratory (SCRL), Department of EEE, Jatiya Kabi Kazi Nazrul Islam University, Mymensingh 2224, Bangladesh.
E-mail addresses: shuaib.eee.iu@gmail.com, shuaibmahmud@jkkniu.edu.bd (S. Mahmud).

https://doi.org/10.1016/j.nxmate.2026.102081
Received 10 January 2026; Received in revised form 8 April 2026; Accepted 11 April 2026
Available online 17 April 2026

perovskite halides [13,14]. The use of this material family is further facilitated by its pronounced compositional flexibility, which can be employed to control the functional characteristics of advanced energy technology [15–19]. In the pursuit of efficient, inorganic double halide perovskites have surged to the forefront of photovoltaic research [20, 21]. More specifically, compounds characterized by the general formula $A_2M^+M^{3+}X_6$, which feature tunable band gaps and outstanding optoelectronic properties, have proven themselves highly adaptable for solar energy applications. For instance, K_2AgAsX_6 (X = Cl, Br) has ideal band gaps of 2.10 and 1.48 eV and relatively low carrier effective masses, making it suitable for photovoltaic absorption [20]. Similar behavior is observed in other materials, including Cs_2AuScX_6 (X = Cl, Br, I) and $Cs_2BiAgBr_6$, both of which exhibit an indirect band gap within the visible part of the spectrum [22,23]. Moreover, the modulation of optical properties through anion substitution is evident in Rb_2AgAsX_6, X = Cl, Br, I, whose band gap continuously decreases from 2.21 to 0.52 eV, illustrating the composition-dependent character of these materials [24]. Similarly, Aslam *et al.* Using DFT, the electronic, optical, and thermoelectric properties of Bi-based double perovskites Cs_2InBiX_6 (X = Cl, Br, I) were explored for solar energy absorption and conversion, revealing favorable optical and thermoelectric properties with a narrow, direct band gap [25]. Using DFT, investigated the structural, optoelectronic, and thermoelectric properties of a range of halide-based double perovskites, Rb_2AlInX_6 (X = Cl, Br, I), finding narrow (1.05, 0.65, and 0.25 eV) and indirect band gaps and promising suitability for optoelectronic devices [26]. The new theoretical power conversion efficiency (PCE) of double perovskite (DP) solar cells has currently reached above 30%, providing the possibility for DP solar cells to be a strong competitor to commercial silicon-based cells [27,28]. The substitution of halides in DPs has triggered materials design efforts and resulted in molecules that have been firmly incorporated into this class of compounds as a prospective class of next-generation renewable energy technologies [29]. Several theoretical and computational works have focused on the intrinsic physicochemical and defect properties of various DP derivatives. Zhang *et al.* [30], Investigated hydrogenated $Cs_2AgBiBr_6$ with a band gap reduction (2.18 eV to 1.64 eV), improved carrier mobility, and energy conversion efficiency of 6.37%. Moreover, with a relatively favorable band gap of 1.6 eV, Cs_2SnI_6 appears to be an excellent light-harvesting material, reaching a PCE of 8% [31]. Garcia-Espejo *et al.* [32], synthesized a new formulation of $Cs_2AgSbBr_6$ as a more stable alternative with a band gap of 1.93 eV. Bhorde *et al.* [33], Rb_2AgBiI_6 has been investigated thus far and shown to be a semiconductor, with a band gap of 1.98 eV. According to Mustafa *et al.* [34], the use of iodine instead of bromine in K_2YAgX_6 (X = Br, I) increases the refractive index, reflectivity, and dielectric constant. Critical thermoelectric parameters, including the power densities and figures of merit, were calculated with the use of the semiclassical Boltzmann theory applied by the BoltzTraP2 code [35]. It is expected that both examined compounds can be used in optoelectronic and thermoelectric devices.

Recently first-principles studies of halide perovskites, double perovskites, and related materials have shed light on structural stability, electronic structure, magnetic interactions, and even thermoelectric transport properties. This topical area has also provided a few studies wherein they highlight the pros and cons of Boltzmann transport characterization in the context of constant relaxation time approximation while computing transport coefficients [36–39]. Inspired by these advancements and to contribute to the ongoing search for high-performance, this work presents a systematic computational investigation of the structural, electronic, optical, and thermoelectric properties of Tl_2AgAsX_6 (X = Cl, I) double perovskites. We systematically investigate properties using the WIEN2k and BoltzTraP2 packages. The optical behavior is characterized via the dielectric function, from which key quantities such as the refractive index, absorption coefficient, and reflectivity are derived. It should be noted that thallium is a highly toxic element, which raises significant environmental and safety concerns, particularly for large-scale device deployment. Therefore, any practical implementation of Tl-based materials would require stringent handling protocols and effective encapsulation strategies to mitigate associated risks. In this context, the present work is intended as a theoretical investigation of the fundamental properties of Tl_2AgAsX_6 compounds, rather than proposing them as environmentally benign photovoltaic materials. The motivation for this study arises from the intriguing electronic structure and favorable optoelectronic characteristics of these materials. Furthermore, the insights obtained here may contribute to a broader understanding of structure–property relationships and support the future design of safer, non-toxic alternative materials with comparable performance.

2. Methodology

First-principles calculations are performed using the Wien2K code that employs the full-potential linearized augmented plane wave (FP-LAPW) method [40]. An iterative scheme was employed, whereby the electronic ground state of the double perovskites under study is calculated. The self-consistent field (SCF) cycle consists of iteratively solving the Kohn-Sham equations until the solution converges. For lattice parameters and bulk modulus, structural optimization was performed using GGA-PBE [41]. Input parameters were charged convergence of 10^{-4} e, energy convergence 10^{-5} Ry, 1000 (10 × 10 × 10) k-points, Fourier expansion maximum charge density (G_{max}) = 12, and muffin tin radius (R_{MT}) × plane wave vector (K_{max}) = 8. Elastic properties confirming the mechanical stability of the materials were calculated using the IR-Elast package coupled with Wien2K [42]. It was used a high k-mesh of 5000 and 10,000 points was used for electronic and optical property calculations. A very well-known computationally cost-effective and accurate method, the TB-mBJ method [43], was employed to calculate accurate band gaps. Photovoltaic efficiency was determined by the use of SCAPS-1D simulation software. Thermoelectric properties were evaluated following the BoltzTraP2 code that takes relaxation time effects into account [44].

3. Results and discussion

3.1. Structural properties and stability

The structural analysis of the compounds Tl_2AgAsX_6 (where X = Cl, I) has indicated that they possess the $A_2M^+M^{3+}X_6$ crystalline structure under the space group Fm-3m (number 225). The cubic structural model and its atomic arrangement are depicted in Fig. 1. It successfully reduced the total energy by optimizing the volume of the unit cell, as shown in Fig. 2. Next to V_o, the framework is highly stable, freezing down to a stable equilibrium state that proves the system is in its ground state. The energy hits its minimum value at the equilibrium volume, E_o, indicating the optimal configuration being assessed. The structural optimization was performed using the GGA-PBE functional, calculating the total energy as a function of volume. For predicting the properties of the material, the lowest energy state of the unit cell is considered the most stable condition in this study. In the case of $Tl_2AgAsCl_6$, we found the energy E_o = -101849.53 Ry to be minimal over all volumes of the simulated cell V_0 = 1859.24 bohr^3 . Similarly, for Tl_2AgAsI_6, the energy and volume at the minima point are E_o = -181739.18 Ry and V_0 = 2653.99 bohr^3 . The energy-volume data were fitted using the Birch-Murnaghan equation of state to obtain the equilibrium parameters. The lattice parameter extracted from our calculations was found to vary from 10.33 Å to 11.59 Å as the size of the halogen atom (Cl, I) was increased. The calculated lattice constants (a_o) and equilibrium parameters are listed in Table 1.

Before conducting an extensive examination of the material's complementary physical and optoelectronic properties, it is necessary to study its stability to assess its suitability for practical applications. The stability of the cubic structure for Tl_2AgAsX_6 (X = Cl, I) was evaluated

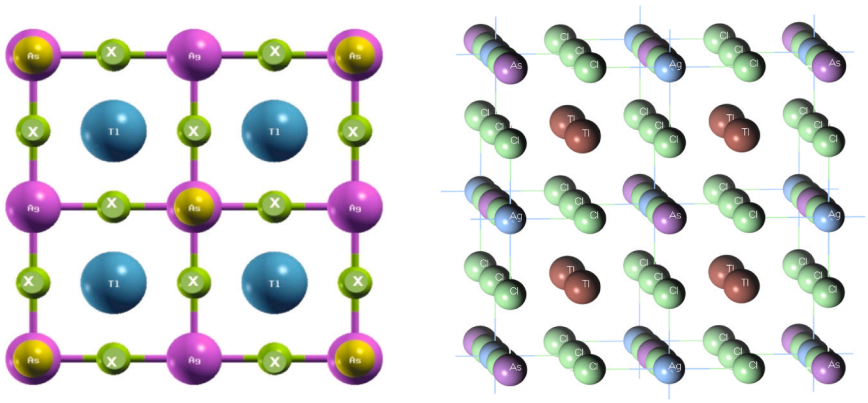

Fig. 1. Unit cell of Tl_2AgAsX_6; (X = Cl, I) 2D and 3D Model.

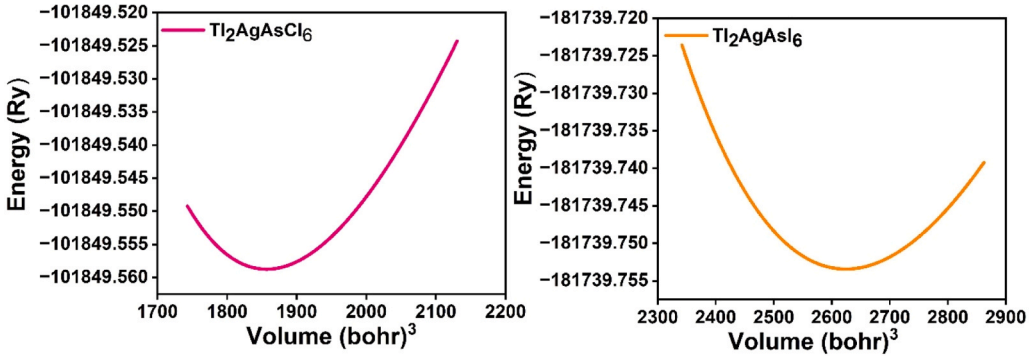

Fig. 2. Varying energy versus volume curve obtained by optimizing the structures of (a) $Tl_2AgAsCl_6$, and (b) Tl_2AgAsI_6.

Table 1
Characteristics and stability-related factors of Tl_2AgAsX_6.

Compounds	a_0 (Å)	V_0 (bohr^3)	E_0 (Ry)	Tolerance Factor, t_G	Octahedral Factor, μ	E_F (eV/atom
$Tl_2AgAsCl_6$	10.33	1859.24	-101849.55	0.93	0.48	-3.49
Tl_2AgAsI_6	11.59	2653.99	-181739.75	0.90	0.40	-3.45

using Goldschmidt's tolerance factor (t_G) and octahedral factor (μ) according to the following equations [45,46]:

$$t_G = \frac{(R_X + R_{Tl})}{\sqrt{2\left(\frac{R_{Ag}+R_{As}}{2} + R_X\right)}} \quad (1)$$

$$\mu = \frac{R_{Ag} + R_{As}}{2R_X} \quad (2)$$

The value t_G between 0.81 and 1.10 typically indicates that the perovskite structure is stable, whereas the μ range of 0.38–0.90 is also considered stable [47,48]. Measured values are 0.93 (X = Cl) and 0.90 (X = I) for t_G, while the μ values are 0.48 (X = Cl) and 0.40 (X = I), which agree with the typical halide perovskite and are also sufficient for stable phases of such compounds. We can thus expect all compounds to crystallize in the cubic perovskite phase because of their suitable tolerance factors.

In addition, to computationally evaluate the level of synthesis feasibility and assess the durability of these DP materials from undergoing spontaneous decay into other binary (or elemental) steps, the energy of formation is derived from [49]:

$$E_F = \frac{E_{Tl_2AgAsX_6} - \left(2E_{Tl} + E_{Ag} + E_{As} + 6E_X\right)}{N} \quad (3)$$

In this equation, $E_{Tl_2AgAsX_6}$ is the total energy of the compound, E_{Tl}, E_{Ag}, E_{As}, and E_X are the energies of the isolated constituent atoms, and N is the number of atoms in the unit cell. The negative E_F values summarized in Table 1 indicate that both compounds are thermodynamically stable. The formation energy becomes less negative from −3.49 eV/atom for the chloride to −3.45 eV/atom for the iodide, suggesting a slight decrease in thermodynamic stability with increasing halide size.

To evaluate the thermodynamic stability of $Tl_2AgAsCl_6$ and Tl_2AgAsI_6, we calculated their formation enthalpies by considering the most probable competing phases. Phase stability is an important criterion for predicting whether a compound can remain stable against decomposition into secondary phases, and thus provides insight into its chemical and thermodynamic stability. The possible competing phases were identified from the Open Quantum Materials Database (OQMD) [50] for the formation enthalpy calculations of each phase as shown in Table 2. The possible decomposition pathway for the studied compounds can be written as:

For Cl-based halides, $Tl_2AgAsCl_6 \rightarrow \frac{2}{5}TlCl + \frac{2}{5}AsCl_3 + \frac{1}{5}AgCl$

For I-based halides, $Tl_2AgAsI_6 \rightarrow \frac{2}{5}TlI + \frac{2}{5}AsI_3 + \frac{1}{5}AgI$

The calculated formation enthalpies of the competing phases were found to be negative, indicating that these materials are energetically favorable with respect to their constituent elements. This negative formation enthalpy supports the thermodynamic stability of $Tl_2AgAsCl_6$

Table 2
Formation energy for possible decomposition/competing phases for the studied compounds.

Compounds	Competing Phases	Formation energy (eV/atom)
$Tl_2AgAsCl_6$	*TlCl*	-1.204
	$AsCl_3$	-0.992
	AgCl	-0.643
Tl_2AgAsI_6	*TlI*	-0.765
	AsI_3	-0.326
	AgI	-0.371

and Tl_2AgAsI_6, suggesting that both compounds may be synthesizable under suitable experimental conditions.

The phonon dispersion curves $Tl_2AgAsCl_6$ and Tl_2AgAsI_6 in Fig. 3(a) and (b) show the underlying lattice vibrational behavior, as well as dynamic stability, of these double perovskite compounds along high-symmetry directions in the Brillouin zone. The fact that phonon branches of both materials keep above the zero-frequency line along the entire path indicates no imaginary frequency, thus ensuring dynamical stability for their crystal structures. At low frequencies, the acoustic modes arise from the Γ point and grow as they approach to zone boundaries, while a few optical modes tend to appear at higher frequencies owing vibrations of constituent atoms. Overall, the comparable lattice dynamics suggested by phonon spectra indicate that both materials are likely to have stable structures and may be explored for potential applications in solid-state and optoelectronic devices.

3.2. Elastic properties

The fundamental elastic constants, C_{11}, C_{12}, and C_{44} are essential to evaluate the mechanical properties of a compound [51]. Fig. 4(a) shows these three essential elastic constants for the cubic perovskites Tl_2AgAsX_6 (X = Cl, I). The perovskites Tl_2AgAsX_6 (X = Cl, I) respect the Born Stability Criterion, so that the conditions $C_{11} - C_{12} > 0$, $C_{11} - 2C_{12} > 0$, $C_{11} > B > C_{12}$, and $C_{44} > 0$ are satisfied [52,53].

This study investigates the mechanical and structural stability of these perovskites. We have calculated the principal elastic parameters, including Anisotropic ratio (A), Bulk modulus (B), Shear modulus (G), Young's modulus (E), Cauchy pressure (C_P), Poisson's ratio (ν), and Pugh's ratio (B/G) all of which are summarized in Fig. 4. The Voigt and Reuss averages were used to calculate the elastic moduli as follows:

$$B = \frac{C_{11} + 2C_{12}}{3} \tag{4}$$

$$G_v = \frac{C_{11} - C_{12} + 3C_{44}}{5} \tag{5}$$

$$G_R = \frac{5C_{44}(C_{11} - C_{12})}{4C_{44} + 3(C_{11} - C_{12})} \tag{6}$$

$$G = \frac{G_v + G_R}{2} \tag{7}$$

$$C_P = C_{12} - C_{44} \tag{8}$$

The shear modulus (G) expresses a material's resistance to shear deformation when subjected to an applied stress and provides insight into its stability against mechanical deformation under extreme conditions. This feature is essential for applications that depend on structural integrity during dynamic loading conditions. Young's modulus (E), a measure of stiffness, is high for these compounds, suggesting significant rigidity and potential stability in device applications, as shown in Fig. 4 (b). Furthermore, the elastic properties of these perovskites are evaluated via Poisson's ratio (ν) and Pugh's ratio (B/G) (Fig. 4(c)) with ν ranging from 0.28 to 0.36 and $B/G > 1.75$, and Cauchy pressure (C_P) (Fig. 4(d)) with values of 14.64 GPa and 2.33 GPa. These values collectively suggest ductile behavior [54–56]. Poisson's ratio (ν) was calculated from the following formula [57]:

$$\nu = \frac{(3B - 2Y)}{6B} \tag{9}$$

A ν value lower than that of many materials indicates a higher resistance to volume change, consistent with the observed shear stiffness. The melting temperature was estimated using the expression $T_m = (553 + 5.911C_{11}) \pm 300K$ [58] and the Debye temperature (Θ_D) was computed using the formula [59]:

$$\Theta_D = \frac{h}{K_B}\left[\frac{3nN_A\rho}{4\pi M}\right]^{\frac{1}{3}} \tag{10}$$

Debye temperatures of 174.31 K and 190.28 K recommend moderate atomic bond strength and thermal stability, which may support energy conversion efficiency in optoelectronic devices. The Longitudinal (V_l) and transversal (V_t) sound velocities are computed from the following well-known relations:

$$V_1 = \sqrt{\frac{C_{11}}{\rho}} \tag{11}$$

$$V_1 = \sqrt{\frac{G}{\rho}} \tag{12}$$

Where, C_{11} is the elastic constant related to longitudinal rigidity, G is the shear modulus, and ρ is the material density, So the average sound velocity (V_m) is calculated as follows:

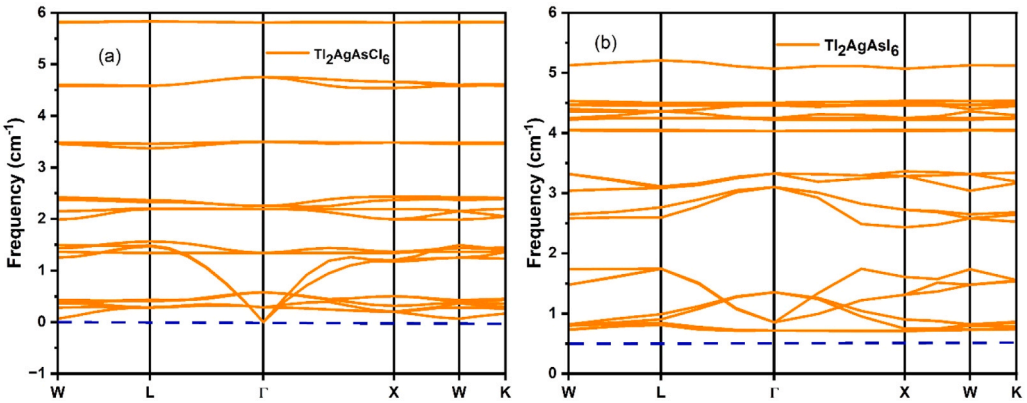

Fig. 3. Calculated phonon dispersion curve of (a) $Tl_2AgAsCl_6$ and (b) Tl_2AgAsI_6.

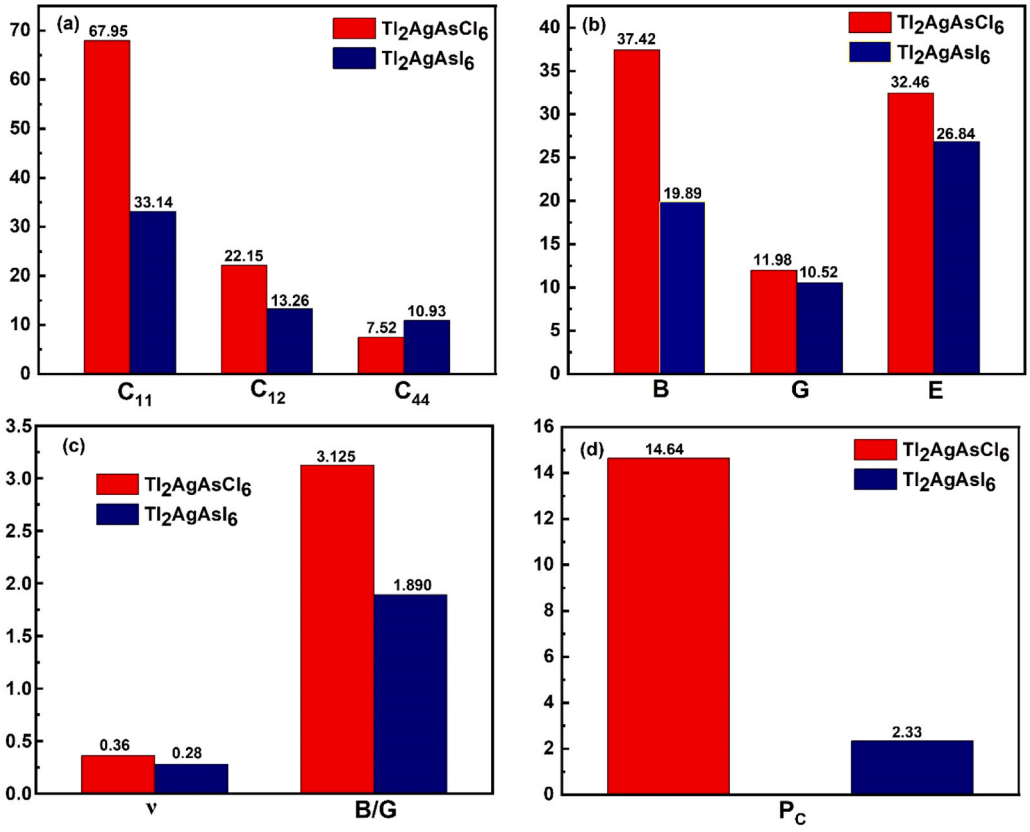

Fig. 4. (a) Elastic Constant (C_{ij}), (b) B (Bulk Modulus), G (Shear Modulus), E (Young Modulus) (c) ν (Poisson Ratio), B/G (Pugh Ratio) and (d) P_c (Cauchy Pressure).

$$V_m = \left[\frac{1}{3}\left(\frac{2}{V_t^3} + \frac{1}{V_l^3}\right)\right]^{-\frac{1}{3}} \tag{13}$$

The lattice contribution of K_L for $Tl_2AgAsCl_6$, and Tl_2AgAsI_6 is calculated according to the well-known Slack's equation [60]:

$$K_L = A\frac{\Theta D^3 V^{\frac{1}{3}} m}{\Upsilon^2 N^{\frac{2}{3}} T} \tag{14}$$

The dependence of K_L on those parameters indicates that, in addition to the atomic-level structure, temperature (T) is crucial for thermal properties. Fig. 11(d) shows the K_L of Tl_2AgAsX_6 vs temperature over the 100–1000 K range, demonstrating their low thermal conductivity and potential utility for thermally stable high-efficiency optoelectronic and photovoltaic devices.

3.3. Electronic properties (Band Gap, DOS, effective mass, charge density distribution)

Density Functional Theory (DFT) calculations are a first-principles method for investigating the electronic properties of materials. These calculations enable researchers to explore various properties, including the band structure, charge carrier mobility, and the density of electronic states, among others. Such electronic properties are essential for distinguishing an insulator from a semiconductor or a conductor. In particular, this distinction depends on the filling of the available energy bands by electrons and the energy band structure of the material [61]. The band structures result for the materials $Tl_2AgAsCl_6$ and Tl_2AgAsI_6 in the energy range from –6 eV to + 6 eV are plotted in Fig. 5. The band structures of both materials show clear analogies and are classified as having indirect band gaps. In such materials, the VBM occurs at X and the CBM occurs at L. The computed band gap energy (TB-mBJ) values for $Tl_2AgAsCl_6$ and Tl_2AgAsI_6 are 1.692 eV and 0.811 eV, respectively. In contrast, the GGA method provides lower band gap values of 0.976 eV ($Tl_2AgAsCl_6$) and 0.234 eV (Tl_2AgAsI_6). The band structures of the materials are determined to be identical, of the indirect band gap type. The energy conversion efficiency in terms of photon absorption of the indirect material is typically lower since the transition from the valence band to the conduction band in indirect materials relies on a phonon-assisted momentum transfer. In this work, we used the TB-mBJ approximation, which is known to be reasonably reliable for band gap estimation and displayed rather good agreement with experimental data. Comparison of GGA and TB-mBJ shows that the TB-mBJ is more accurate than GGA in reproducing energy gaps [62]. The inclusion of spin–orbit coupling (SOC) leads to a slight reduction in the band gap with only minor changes in the band dispersion near the band edges, which is consistent with previous first-principles studies on Tl-based and halide perovskite materials [22,63,64].

We show that the charge carrier effective mass in the double perovskites examined is a measure of how the carriers (electrons or holes) responds to external perturbation as it traverses the crystal lattice. Lower effective mass thus means the carrier moves more easily in the effective electric field, leading to increased charge transport and improved device performance as a result. The effective mass can be calculated by the associated expression, through the second derivatives of energy E with respect to momentum K that describe the curvature of edges of the bands [65].

Table 3
Thermal properties of the investigated compounds.

Parameters	$Tl_2AgAsCl_6$	Tl_2AgAsI_6
Anisotropy factor A	0.64	0.005
Average wave velocity V_m (ms^{-1})	1768.28	1511.26
Debye temperature θ_D (K)	174.31	190.28
Melting Temperature ($\pm$ 300K)	954.64	748.92
Lattice Thermal Conductivity, K_L (300 K)	0.25	0.17

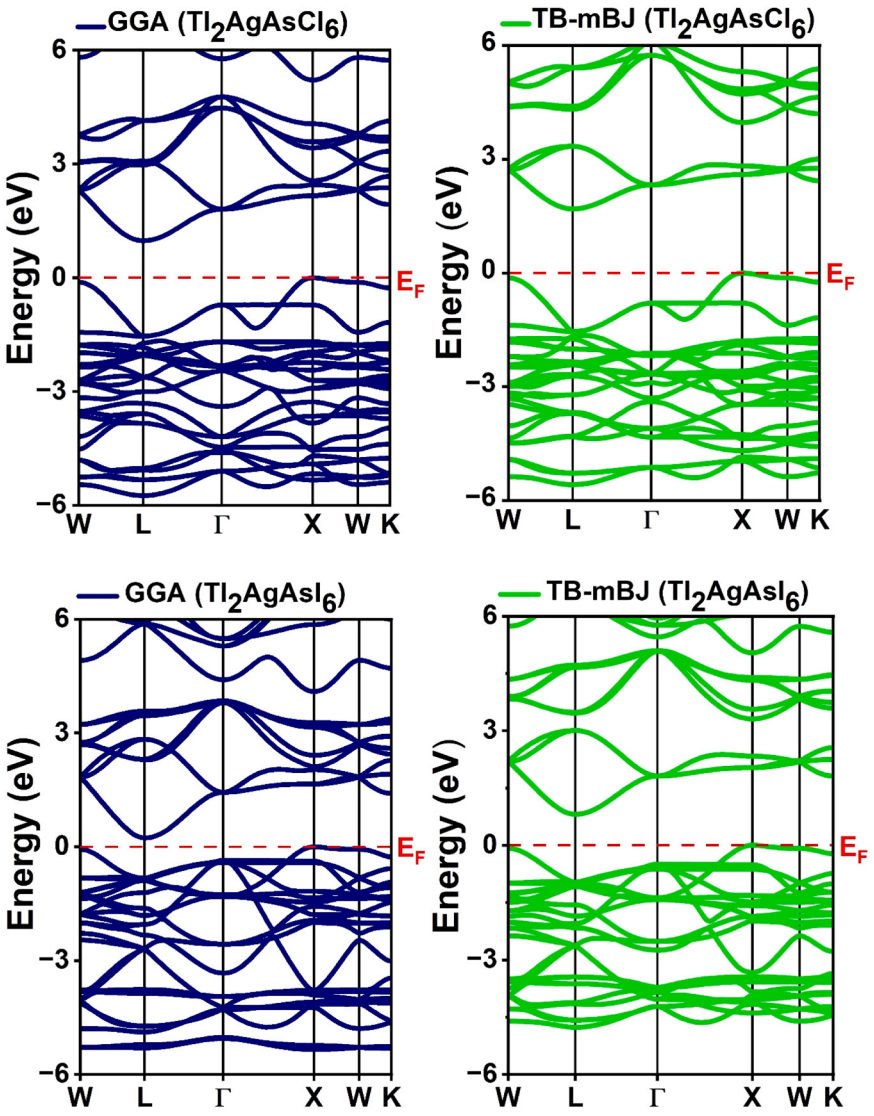

Fig. 5. Band figure of Tl_2AgAsX_6 (X = Cl, I), estimated GGA–PBE (left side) and TB-mBJ (right side) techniques.

$$\frac{1}{m^*} = \frac{1}{h^2}\frac{d^2E}{dK^2} \tag{15}$$

Studying its electrical properties requires an examination of its charge carriers (electrons and holes). The electrons in these materials are capable of high mobility, with an effective electron mass of 0.17 for $Tl_2AgAsCl_6$ and 0.09 for Tl_2AgAsI_6. Such materials may also be of interest for optoelectronic applications due to their properties correlated with the beneficial band gap range and the high absorption characteristics of these materials in the visible range necessary for photon capture and electron excitation. The value of the exciton binding energy $\left(E_b^{ex}\right)$ plays an important role in determining the suitability of the studied double perovskites for solar cell purposes. As for efficient charge separation, it requires low binding energy so as to allow excitons (electron-hole pairs) to dissociate to free carriers (electron and hole) with room-temperature thermal energy. An enhancement of exciton binding energy can impede their dissociation, thus limiting the charge carrier diffusion length and increasing the recombination rate, resulting in a loss in device performance in solar cells. Excitonic effects are driven by the Coulomb interaction between photo-excited electrons and holes.

Using the associated mathematical expression, the Wannier–Mott exciton model is applied to determine E_b^{ex} for the Tl_2AgAsX_6 (X = Cl, I) double perovskites owing to their relatively large dielectric constants.

$$E_b^{ex} = \frac{\mu_r\, e^4}{32\left(\pi\varepsilon_0\varepsilon_x\, h^2\right)} = 13.56 \quad \frac{\mu_r}{m_e\ \varepsilon_1(0)^2} \text{where} \mu_r = \frac{m_e^* \quad \times m_h^*}{m_e^* \quad + m_h^*} \tag{16}$$

We apply the Wannier–Mott model to estimate the exciton binding energy using the calculated effective masses and dielectric constants. The typical application of this model is at materials with high dielectric screening, like halide perovskites. The calculated values in Table 4 show a low exciton binding energy which allowed the easy dissociation of exciton into free carrier. Nonetheless the model gives only a rough estimate since it does not directly include the fine details of the band structure nor the electron–hole interactions. More rigorous many-body approaches, such as calculations based on the Bethe–Salpeter equation (BSE), would be required for a more accurate description of excitonic effects and the optical absorption onset. In addition, the estimated effective density of states in the valence (N_v) and conduction (N_c) bands are estimated from:

$$N_v = 2.5409 \times 10^{19}\left(m_h^*/m_0\right)^{\frac{3}{2}} \tag{17}$$

$$N_c = 2.5409 \times 10^{19}\left(m_e^*/m_0\right)^{\frac{3}{2}} \tag{18}$$

The values shown in Table 4 indicate that an increased effective mass enhances the density of states in the related band and, thereby, drives

Table 4
Computed band gaps, effective masses of charge carriers and mobility of studied compounds.

Compounds	Band Gap (eV) by TB-mBJ	Effective mass		E_b^{ex}	N_c	N_V	μ_e	μ_h
		m_h^*	m_e^*					
$Tl_2AgAsCl_6$	1.692	0.26	0.17	0.368	1.78×10^{18}	3.36×10^{18}	103.43	67.63
Tl_2AgAsI_6	0.811	0.27	0.09	0.163	6.86×10^{17}	3.56×10^{18}	195.36	65.12
$K_2CuBiCl_6$ [66]	1.53	–	–	–	–	–	–	–
$Rb_2AuScBr_6$ [22]	1.70	0.27	0.14	–	–	–	–	–
Cs_2AuSbF_6 [67]	1.74	0.72	0.25	1.12	–	–	–	–

the concentration and transport properties of carriers in semiconductors [63]. The mobility of charge carriers (μ) indicates the speed of electrons or holes in moving through a semiconductor material due to an electric field. It is mathematically expressed as:

$$\mu_e = \frac{q\tau}{m_e^*} \text{and} \mu_h = \frac{q\tau}{m_h^*} \quad (19)$$

where q is the elementary charge, τ is the mean free relaxation time between successive scattering events, and m is the effective mass of the carrier. For electrons, it is μ_e, d for holes μ_h values are displayed in Table 4. Higher mobility indicates that charge carriers can move more freely, enhancing the material's conductivity.

Fig. 6 presents the total density of states (TDOS) and partial density of states (PDOS) for $Tl_2AgAsCl_6$ and Tl_2AgAsI_6, revealing the orbital contributions to the electronic structure. The TDOS profiles are similar in shape but shifted due to differences in halogen size and electronegativity. In $Tl_2AgAsCl_6$, the valence band maximum (VBM) is dominated by Ag-d and Cl-p states, while the conduction band minimum (CBM) is primarily composed of As-p and Tl-s/p orbitals. In contrast, Tl_2AgAsI_6 shows a VBM dominated by Ag-d and I-p states, with the CBM again formed by As-p and Tl-s/p. The larger atomic radius and lower electronegativity of I reduce orbital overlap, which raises the VBM and leads to a smaller band gap in Tl_2AgAsI_6 compared with $Tl_2AgAsCl_6$. Conversely, the smaller Cl atom promotes stronger hybridization and stabilizes the VBM at lower energy, resulting in a wider band gap in $Tl_2AgAsCl_6$. The PDOS further highlights that Ag-d states contribute most intensely near the VBM in both compounds, while As-p states dominate the CBM. These orbital interactions directly govern the optoelectronic properties, including band gap tuning via halogen substitution.

3.4. Charge density mapping

Charge density mapping in materials such as Tl_2AgAsX_6 (X = Cl, I) explores structural and electronic localization in the unit cell. The type of bonding of the atoms and functional properties are determined by performing an electron density map analysis. Regions of low electron density may reflect ionic character, while peaks of high electron density between atoms correspond to covalently bonded regions. Charge density maps of $Tl_2AgAsCl_6$ and Tl_2AgAsI_6 represent how the charge is distributed between atoms of Tl, Ag, As, and X (Cl, I). Charge density mapping indicates that the As–Cl bond displays significantly display a significantly stronger covalent character than the As–I bond, as indicated by the enhanced charge density localization on the As atom (+4.6042).

It is this enhanced bonding that renders $Tl_2AgAsCl_6$ relatively stable with lower (more negative) formation energy compared to Tl_2AgAsI_6. Due to the size of Tl^+ and its tendency to donate electrons, it has a low electron density (≈ +0.0008). Unlike Ag^+, for which the electron density surrounding it is high (maximum value +4.6042), indicating a high

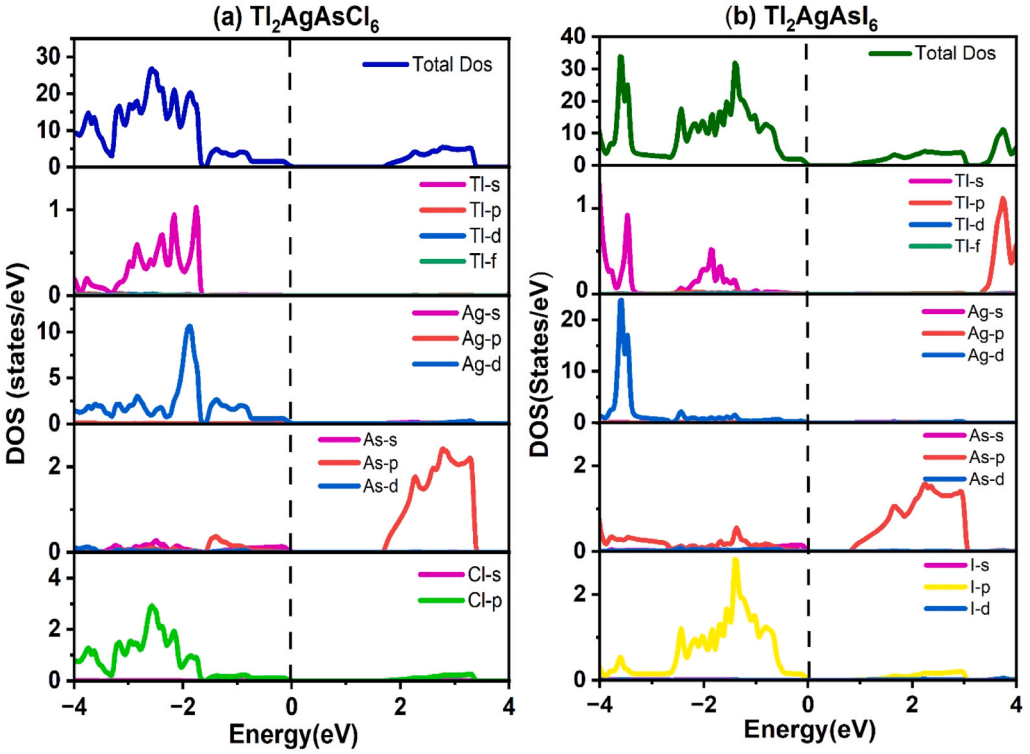

Fig. 6. TDOS and PDOS plots of (a) $Tl_2AgAsCl_6$ (b) Tl_2AgAsI_6.

ability to attract electrons, As^{3+} reflects the degree of participation of electrons in the bond formed; As^{+} has a higher degree when participating with a ligand of Cl or I. The valence states show lower charge density for As compared to Ag, while Ag–Cl shows a strong covalent character (up to a maximum value +4.6042). Both As–Cl and As–I also exhibit covalent bonding. However, As–Cl presents a stronger covalent character compared to As–I, which has some ionic character. For covalent interaction, $Tl_2AgAsCl_6$ (up to +4.6042) has a very strong nature similar to Tl_2AgAsI_6 (up to +4.5834). In combination with favorable electronic properties contributed by these interactions, these materials are suitable for the design of high electron mobility and efficient charge transfer features required in optoelectronic and thermoelectric applications. Hence, the charge density distributions illustrated here correspond to the actual electronic structure associated with the ionic and covalent domains within the crystal structure of these double perovskite halide materials from the Tl_2AgAsX_6 family that were explored in the present work (Fig. 7).

3.5. Optical properties

The optical properties of a material, specifically the absorption and release to light, are intrinsically fundamental in deciding the potential of such a material to be exploited for optoelectronic and photovoltaic applications. This assembly of properties provides critical insights into the material's light feedback and is directly correlated with its suitability for applications. Fulfilling this goal requires knowledge of the material's electronic structure and optical behaviour. The optical properties of Tl_2AgAsX_6 (X = Cl, I) calculated within the TB-mBJ approximation using first-principles methods for photon energies from 0 to 6 eV are shown in Fig. 8(a)–(h). The dielectric function is critical in elucidating the light-harvesting performance of double perovskite compounds. The complex dielectric constant can usually be written as:

$$\varepsilon(\omega) = \varepsilon_1(\omega) + i\varepsilon_2(\omega) \tag{20}$$

Where ω is the angular frequency of the incident light, the dielectric function's real part, $\varepsilon_1(\omega)$, is a measurement of a material's ability to store electrical energy in it and contribute to its refractive properties. The imaginary part $\varepsilon_2(\omega)$ describes the electronic transitions in the band structure of the material that are responsible for energy losses and absorption at different photon energies, illustrated in Fig. 8**(a) and (b)**. This information altogether offers a clear picture of the optical response of the material, obtained using the Kramers–Kronig relation [68]. The static dielectric constant $\varepsilon_1(0)$ for $Tl_2AgAsCl_6$ and Tl_2AgAsI_6 are 4.7 and 7.86, respectively, demonstrating a strong polarization response that is critical for light absorption. $\varepsilon_1(0)$ shows the maximum value and then decreases as photon energy (eV) increases. The peak shifts downward when the halogen atoms change from Cl to I.

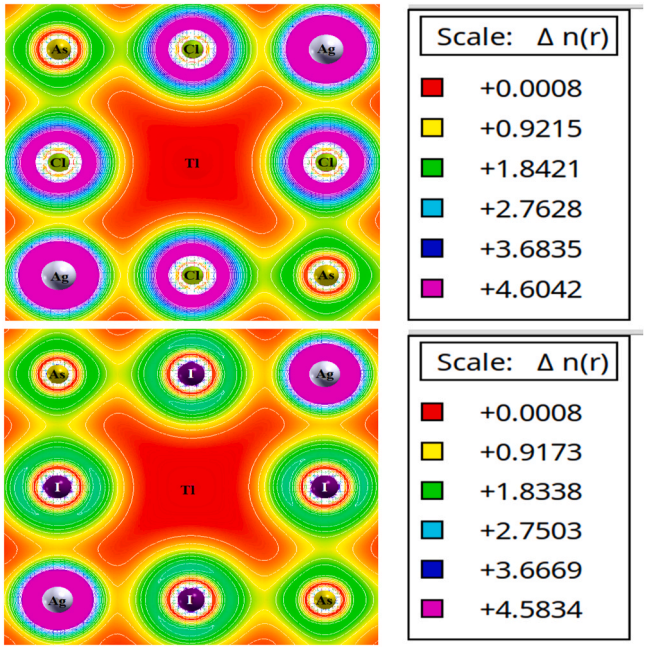

Fig. 7. Charge density mapping of $Tl_2AgAsCl_6$ and Tl_2AgAsI_6 (2D view).

The maximal peaks of $\varepsilon_1(\omega)$ are located at 2.62 eV and 1.80 eV with corresponding peak values of 9.57 and 14.27, respectively. Using the Penn model, which simplifies scattering events in semiconductors via the nearly-free-electron approximation, the static dielectric constant can also be estimated as:

$$\varepsilon_1(0) = 1 + (E_{hop} / E_g)^2 \tag{21}$$

The main absorption in $\varepsilon_2(\omega)$, occurs between 1 and 3.5 eV, corresponding to the visible light region, with values of 7.58 and 12.78 for $Tl_2AgAsCl_6$ and Tl_2AgAsI_6, respectively. These results indicate promising dielectric properties for photovoltaic light absorption [69]. The static refractive index $n(0)$ defines the balance between the speed of light and material density, measuring 2.17 for Cl and 2.80 for I; values that are suitable for efficient light transmission and optoelectronic applications. Higher refractive indices improve light absorption and photon–material interactions, enhancing the efficiency of photovoltaic energy conversion.

The frequency-dependent refractive index $n(\omega)$ ranges from 3.15 for $Tl_2AgAsCl_6$, and 3.85 for Tl_2AgAsI_6 (see Fig. 8**c**); the trend indicates stronger optical confinement for the I-based compound. As previously noted, $n(\omega)$ is directly related to the real part of the dielectric function through $\varepsilon_1(\omega) = n^2(\omega)$. Similarly, the extinction coefficient $k(\omega)$ which quantifies the attenuation of light within the material, follows the behavior of the imaginary component $\varepsilon_2(\omega)$, as presented in Fig. 8**(d)**. This confirms high absorption capability of the materials, thus confirming their promise in photovoltaic applications.

The optical absorption coefficient $\alpha(\omega)$ is a key parameter for measuring the optical performance of optoelectronic materials. $\alpha(\omega)$ is vitally important for solar energy conversion efficiency, as it represents the amount of light absorbed per unit length of the material at a given wavelength. An increase in $\alpha(\omega)$ means better optical transition probability for the changeover of electrons from valence bands to conduction bands and this parameter is specified as follows [72]:

$$\alpha(\omega) = \sqrt{2}\left[\sqrt{\varepsilon_1(\omega)^2 + \varepsilon_2(\omega)^2} - \varepsilon_1(\omega)\right]^{\frac{1}{2}} \tag{22}$$

In Fig. 8(e), the $\alpha(\omega)$: 6.07 × 10^5 cm^{-1} at 3.52 eV for $Tl_2AgAsCl_6$ and 6.05 × 10^5 cm^{-1} at 2.76 eV for Tl_2AgAsI_6. As the X-site halide changes from Cl to I, the $\alpha(\omega)$ increases in magnitude and exhibits a redshift in peak energy in the visible light. This absorption behavior aligns with that of conventional crystalline solar materials such as GaAs and Si [73]. The absorption behavior is further compared with the electronic band gaps. $Tl_2AgAsCl_6$ (1.692 eV) and Tl_2AgAsI_6 (0.811 eV) exhibit strong absorption (~10^5 cm^{-1}) at higher energies of 3.52 eV and 2.76 eV, indicating that optical transitions occur well above the band edge. This is typical of indirect semiconductors, where near-edge absorption is weak due to phonon-assisted transitions, while higher-energy absorption remains significant for efficient light harvesting. The bandgap-related energy shift (3.52 eV for Cl to 2.76 eV for I) evidences a tunable bandgap, providing versatility for targeted applications across spectral ranges. The other important physical quantity for light absorption is the optical conductivity $\sigma(\omega)$, which describes the motion of charge carriers driven by light-matter interactions in optoelectronic materials, $\sigma(\omega)$ in Fig. 8(f), shows a trend similar to the $\alpha(\omega)$. The order of $\sigma(\omega)$ corresponding to their absorption peaks around 3.52 eV and 2.76 eV confirms that materials have high $\sigma(\omega)$ in the visible light spectrum. Optical reflectivity $R(\omega)$, determines the fraction of incoming

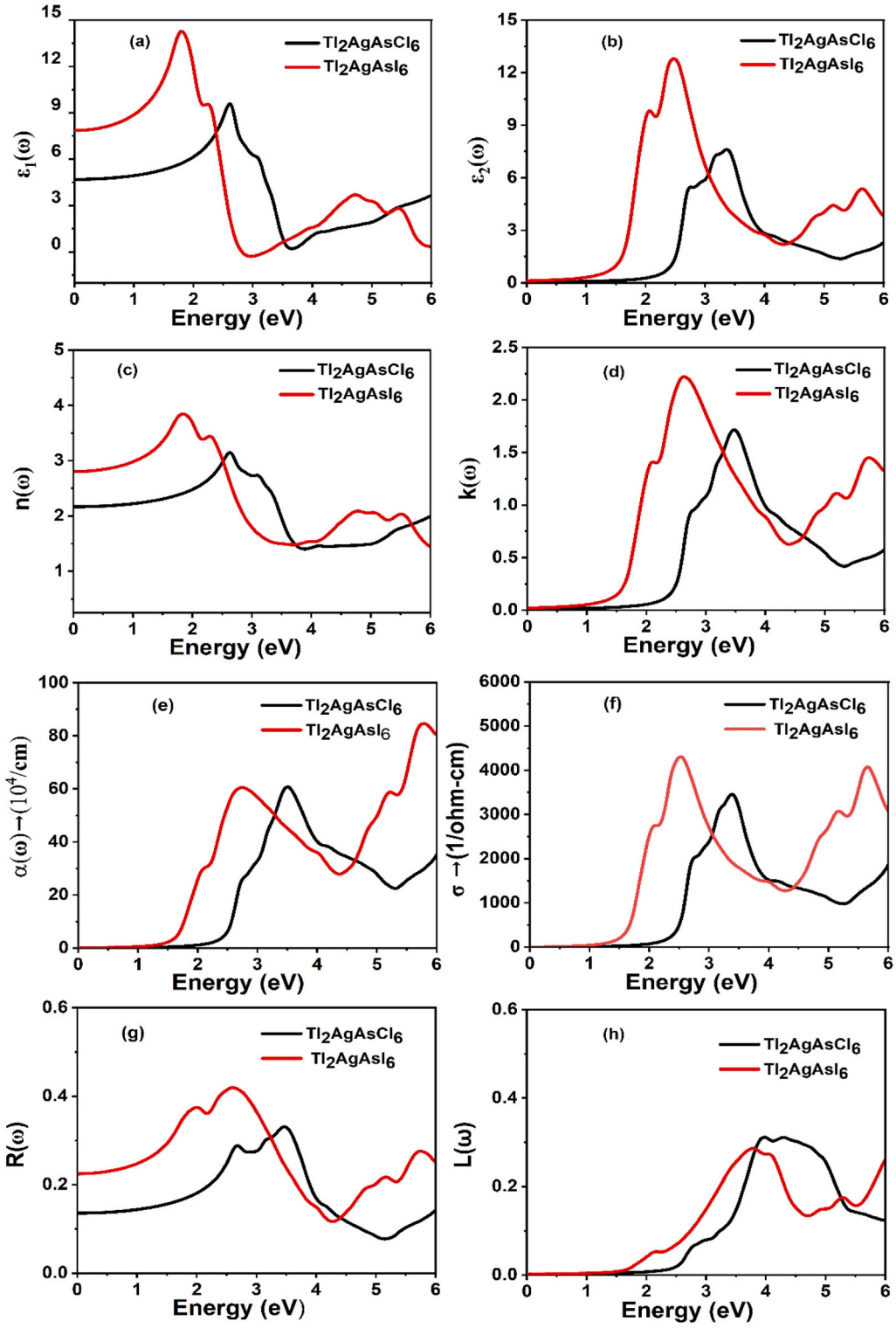

Fig. 8. (a) $\varepsilon_1(\omega)$, (b) $\varepsilon_2(\omega)$, (c) $n(\omega)$, (d) $k(\omega)$, (e) $\alpha(\omega)$, (f) $\sigma(\omega)$, (g) $R(\omega)$, and (h) $L(\omega)$.

light reflected from the surface of the material. The light energy spectrum has three main parts: absorption, transmission, and reflection. The results are shown in Fig. 8(g), where $R(\omega)$ is plotted, values are summarized in Table 5 and show consistently low values (mostly below < 43%) across the spectrum range. In the visible region, $Tl_2AgAsCl_6$ reaches a maximum photovoltaic reflection of 33% at 3.0 eV, with Tl_2AgAsI_6 reaching a maximum of 43% at 2.2 eV. The materials also have reduced reflectivity 32.7% and 40.9% at energies of their corresponding band gaps (3.52 eV for Cl and 2.76 eV for I). The low reflectivity especially in the visible region means that few photons are lost, and these materials prove nearly ideal for photovoltaic solar cells.

In Table 5, we compare the TB-mBJ optical properties of Tl_2AgAsX_6 (X = Cl, I) with that of other lead free double perovskites. The static dielectric constants are 4.7 and 7.86 and the maximum absorption coefficients reach 6.07×10^5 cm^{-1} (3.52 eV) and 6.05×10^5 cm^{-1} (2.76 eV), respectively, for the Cl and I compound. Indeed, these

Table 5
Calculated optical properties of studied materials.

Compounds	$\varepsilon_1(0)$	Maximum $\varepsilon_1(\omega)$ at eV	$n(0)$	Maximum $n(\omega)$ at eV	$\alpha_{max}(\omega)$ cm^{-1} at eV	$R(0)$	Ref
$Tl_2AgAsCl_6$	4.7	9.57 (2.62 eV)	2.17	3.15 (2.62 eV)	6.07×10^5 (3.52 eV)	0.14	This work
Tl_2AgAsI_6	7.86	14.27 (1.80 eV)	2.80	3.85 (1.86 eV)	6.05×10^5 (2.76 eV)	0.23	This work
$Cs_2AuInCl_6$	3.80	–	1.95	–	2.24×10^5	0.10	[70]
Cs_2AuInF_6	3.64	–	1.90		3.21×10^5	0.09	[70]
$Rb_2AuScCl_6$	3.19	–	1.79	–	–	0.07	[22]
$Li_2AgAsCl_6$	7.50	–	2.73	–	–	0.216	[71]

values are similar or even surpass those of $Li_2AgAsCl_6$ and other related double perovskites. Similar trends in absorption coefficients ($\sim 10^4$–10^5 cm^{-1}) and dielectric response have also been reported for related halide double perovskites, supporting the reliability of the present results [66]. The energy loss function $L(\omega)$ is shown in Fig. 8(h), which provides information about $L(\omega)$ of electrons traveling through the electronic structure of the material. This enables information about plasmonic resonances and collective electron gas oscillations, the collective interaction of electrons with the electromagnetic field, to be extracted to describe the response of the material to electromagnetic perturbations [74]. Loss spectrum peaks corresponding to plasma frequencies show no strong $L(\omega)$ peaks below the band gaps of the compounds. In the range of 0–4 eV, the maximum $L(\omega)$ are as follows: for $Tl_2AgAsCl_6$, 0.31; for Tl_2AgAsI_6, 0.28. For energies higher than 5 eV, decreases gradually, remaining below 0.26. The materials are particularly efficient (0–4 eV) because of the relatively lower losses in the visible spectrum, making them applicable to photovoltaic cells and photodetectors.

In conclusion, the deep analysis of optical parameters $\varepsilon(\omega)$, $\alpha(\omega)$, $\sigma(\omega)$, $R(\omega)$, and $L(\omega)$ shows that they exhibit excellent polarizability, absorption, and large optical conductivity in the visible region. This fast absorption, conductivity, and polarizability, along with low reflectivity and optical losses, confirm the potential of Tl_2AgAsX_6 as absorber-layer materials for solar cells, providing a tunable bandgap for potential photovoltaic applications.

3.6. Photovoltaic properties

The designed double perovskite solar cell includes $Tl_2AgAsCl_6$ and Tl_2AgAsI_6 absorbers in a co-packed device structure with an ETL (electron transport layer), HTL (hole transport layer), and back contact in Fig. 9. The initial cell design involves two devices, the first using $Tl_2AgAsCl_6$, V_2O_5 as the HTL, and SnO_2 as the ETL; the other cell design uses Tl_2AgAsI_6, CBTS as the HTL,WS_2 as the ETL. The configuration uses an n–i–p arrangement, which is notable for its improved response to longer-wavelength light over a standard p–n junction. Within this n–i–p architecture, the depletion region exists well into the device deep inside the intrinsic layer, resulting in an effective charge separation and collection [75]. The selection of transport layers was guided by quantitative band alignment, carrier transport capability, and material stability, which collectively govern interfacial charge transfer and recombination dynamics. For the $Tl_2AgAsCl_6$-based device, the absorber exhibits CBM and VBM positions at −4.34 eV and −6.03 eV, respectively. The chosen ETL, SnO_2, possesses a CBM of approximately −4.0 eV, resulting in a conduction band offset (CBO) of ∼0.34 eV, which lies within the optimal range (0–0.4 eV) for efficient electron extraction while suppressing hole backflow. Additionally, SnO_2 offers high electron mobility (10–240 $cm^2\ V^{-1}\ s^{-1}$), wide band gap (>3.6 eV), and excellent chemical stability, ensuring minimal parasitic absorption and long-term device reliability. On the HTL side, V_2O_5 with a VBM of −6.2 eV provides a favorable valence band offset (VBO ∼ 0.17 eV) relative to the absorber, enabling efficient hole extraction and reduced interfacial recombination. For the Tl_2AgAsI_6-based device, the absorber CBM and VBM are positioned at −4.22 eV and −5.03 eV, respectively. WS_2 is employed as the ETL due to its CBM (-3.9 eV), yielding a moderate CBO (∼0.32 eV) that facilitates efficient electron transport. WS_2 further exhibits good carrier mobility and strong environmental stability, which are beneficial for sustained device operation. The HTL CBTS (Cu_2BaSnS_4), with a VBM of −5.5 eV, forms a suitable VBO (∼0.47 eV), promoting effective hole extraction while maintaining a barrier against electron leakage. Moreover, CBTS is composed of earth-abundant, non-toxic elements and demonstrates good thermal and chemical stability, aligning with sustainable device design. The resulting band alignment in both device configurations corresponds to a staggered (type-II) heterojunction, ensuring directional carrier transport, where

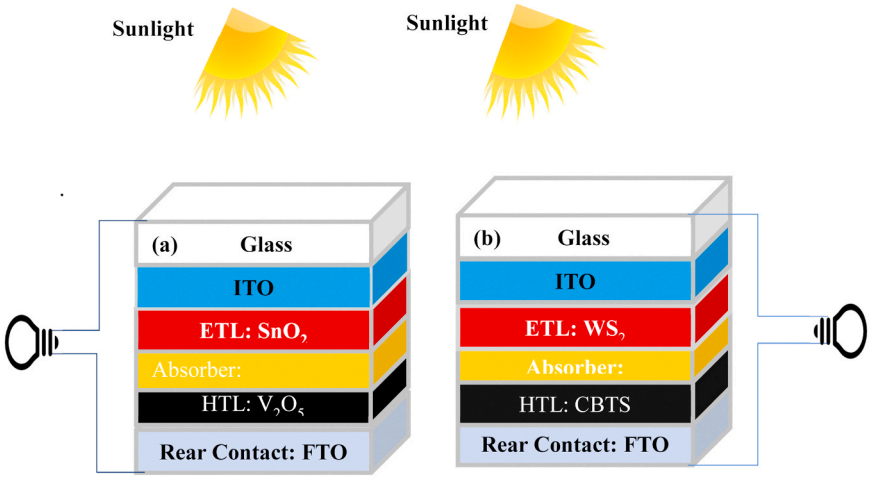

Fig. 9. Design configuration of (a) $Tl_2AgAsCl_6$ and (b) Tl_2AgAsI_6 based DPSC.

electrons are selectively transferred to the ETL and holes to the HTL. This alignment minimizes interfacial recombination losses and enhances charge collection efficiency, thereby supporting the high simulated photovoltaic performance. For comparison, alternative ETLs such as TiO_2, ZnO, and PCBM, and HTLs including Spiro-OMeTAD, NiO_x, and CuSCN, may also provide suitable band alignment. However, the selected combinations demonstrate a more balanced integration of band offset (0.17–0.47 eV), carrier mobility, optical transparency, and material stability, making them more favorable for the present device architecture.

The absorbers have an indirect band gap, which means that the absorption near the band edge is weaker, leading to thicker absorber layers to provide enough carrier generation. Hence, thickness optimization in the SCAPS simulations is one of the key elements to obtain the examined device performance.

The judicious selection of Electron Transport Layers (ETL) and Hole Transport Layers (HTL) is imperative for maximizing carrier extraction and minimizing interfacial recombination. To justify the device architectures utilizing SnO_2/V_2O_5 for $Tl_2AgAsCl_6$ and WS_2/CBTS for Tl_2AgAsI_6 the absolute band edge alignments relative to the vacuum level were evaluated based on the electron affinity and band gap parameters inputted into the SCAPS-1D model. An optimal interface requires a favorable Conduction Band Offset (0–0.3 eV) at the Absorber/ETL interface to facilitate electron transfer while blocking holes, and a favorable Valence Band Offset (sufficient for hole extraction without forming recombination-prone cliffs) at the HTL/Absorber interface for efficient hole extraction.

For the $Tl_2AgAsCl_6$ absorber (Eg = 1.692 eV), the estimated electron affinity is 4.340 eV, positioning its conduction band minimum (CBM) at −4.340 eV and its valence band maximum (VBM) at −6.032 eV. SnO_2 was selected as the ETL because its CBM of −4 eV creates a favorable CBO that allows barrier-free electron injection. Correspondingly, V_2O_5 provides an excellent HTL match with a VBM of −6.2 eV, establishing a strong energetic driving force for hole extraction. Similarly, for the $Tl2_2AgAsI_6$ device (Eg = 0.811 eV, 4.220 eV, WS_2 and CBTS were chosen as

the ETL and HTL, respectively. The CBM of WS_2 −3.95 eV and the VBM of CBTS −5.5 eV form a well-matched, cascaded energy level alignment with the absorber. This optimal band alignment is critical in suppressing non-radiative recombination at the interfaces and serves as the fundamental physical basis for the high photovoltaic parameters extracted from the simulation. Band alignment in this work is based on electron affinity values governed in SCAPS-1D while the direct first-principles calculation gives the vacuum-referenced band edge positions. Based on their electron affinities, $Tl_2AgAsCl_6$ (4.34 eV) and Tl_2AgAsI_6 (4.22 eV), in combination with SnO_2 (4.5 eV) and WS_2 (3.9 eV), can provide conduction band offsets of ~0.16–0.32 eV, which may be ideal for electron extraction. Although this is a commonly used approach in device simulations, it has a semi-empirical nature to the analysis. The band bending thus detected does not permit a more accurate evaluation of absolute band edge positions without vacuum-level alignment through surface based DFT calculations, something we deem to be out of the scope of the present work. Thus, the suggested band alignment should be considered as a physically credible approximation for the device-level performance investigation. Double perovskite solar cells (DPSC) consisting of absorbers showcase differing photovoltaic responses as indicated by their J–V characteristics displayed in Fig. 10 (a) which provide basic, but significant knowledge of photovoltaic parameters including short-circuit current density (Jsc), open-circuit voltage (Voc), and fill factor (FF) for analysis of the optimized performance of solar cells.

It must be emphasized that the simulated power conversion efficiencies of 23.38% and 16.76% for $Tl_2AgAsCl_6$ and Tl_2AgAsI_6, respectively, are highly dependent on the initial parameters assumed within

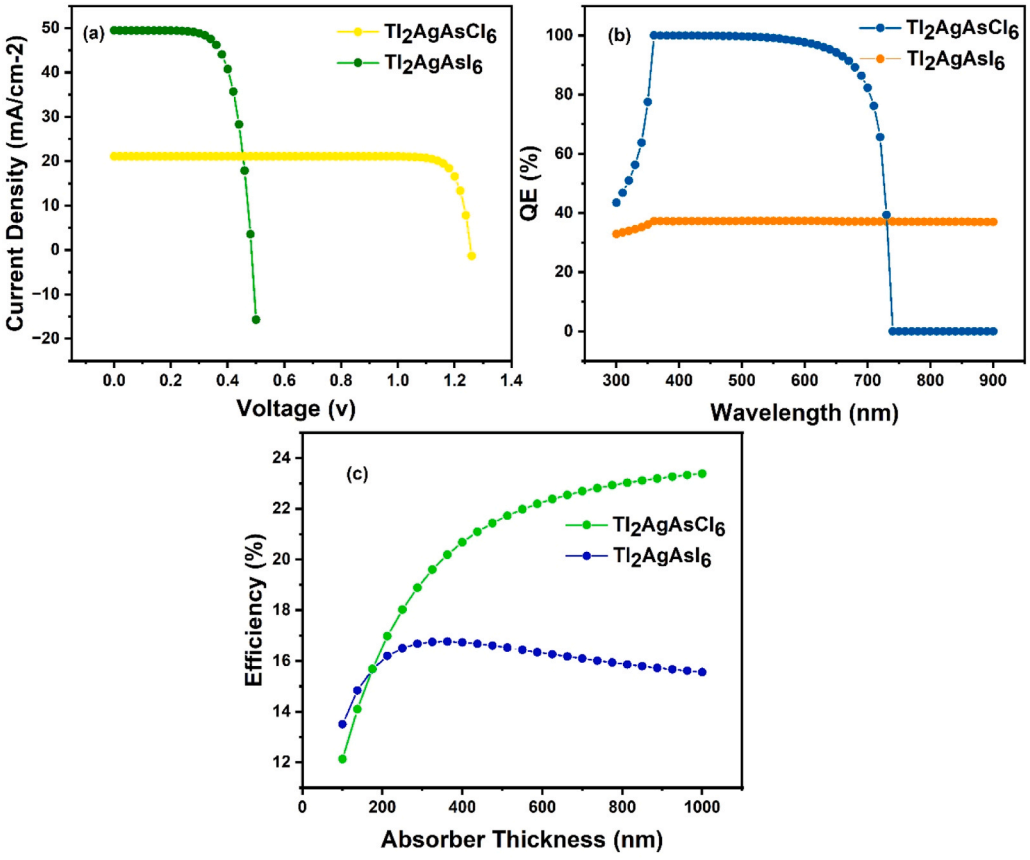

Fig. 10. (a) Current density vs Voltage (b) QE vs Wavelength (c) Efficiency vs Absorber Thickness.

the SCAPS-1D model. Because macroscopic variables such as bulk defect densities, interface trap states, and transport layer carrier concentrations are not directly derived from our first-principles DFT calculations, the reported PCEs should be interpreted as idealized theoretical upper bounds rather than realistic predictive values. The device performance is highly sensitive to these assumptions; in practical fabrication, deviations such as higher deep-level trap densities or suboptimal doping in the transport layers will inevitably accelerate non-radiative recombination and diminish the open-circuit voltage (*Voc*) and fill factor (FF). Therefore, while the systematic tuning of the absorber thickness demonstrates the intrinsic light-harvesting limits of these materials, future experimental efforts must strictly focus on defect passivation and carrier concentration optimization to approach these theoretical efficiency ceilings. The first device gives a curve of J_{SC} = 21.10 mA/cm^2, V_{OC} = 1.26 V, FF = 86.64% and PCE = 22.99% at 800 nm due to efficient charge-separation with low recombination at the interfaces. On the other hand, the corresponding second device configuration shows J_{SC} = 49.46 mA/cm^2, V_{OC} = 0.48 V, FF = 69.98% and PCE = 16.76% at 362.6 nm, owing to a stronger light absorption but being limited by recombination losses [76]. The quantum efficiency (QE) in Fig. 10**(b)** of the DPSC shows its spectral response. The QE for the $Tl_2AgAsCl_6$ based DPSC reaches a maximum of 99.99% between 360–400 nm, which increases from 43.51% at 300 nm and zero contribution beyond 740 nm, consistent with a wide bandgap restricting long-wavelength absorption. For the Tl_2AgAsI_6 based DPSC, the QE is highest (37.32% around 380–400 nm), starting at 32.88% at 300 nm and gradually decreasing to 36.98% at 900 nm with broader spectral response owing to its narrower bandgap [77]. The efficiency of $Tl_2AgAsCl_6$ sharply increases from 12.13% at 100 nm to 22.99% at 800 nm and reaching a maximum of 23.38% at 1000 nm, benefiting from high absorption and low recombination, which suggests this material is a good candidate for use in thick-layer solar cell; this rise occurs because thicker absorbers capture more long-wavelength photons while minority carriers remain effectively collected due to long diffusion lengths. while Tl_2AgAsI_6 achieves 16.76% at 362.6 nm, the photocurrent density drops to 15.88% at 800 nm due to recombination losses, making thin-film application a better option; the decline reflects increased bulk recombination in thicker layers, where photogenerated carriers recombine before reaching the junctions. These trends are shown in Fig. 10(c). It should be emphasized that device performance is highly sensitive to bulk and interfacial defect densities. In the present simulations, the absorber defect density is fixed at 10^{15} cm^{-3}, and the interface defect density is maintained at 1×10^{10} cm^{-3} with capture cross-sections ranging from 10^{-17} to 10^{-19} cm^2, representing near-ideal conditions. A qualitative sensitivity analysis indicates that increasing the absorber defect density to 10^{17} cm^{-3} would significantly enhance trap-assisted recombination, leading to a reduction in open-circuit voltage and fill factor, and consequently lowering the overall PCE. Similarly, increasing the interface defect density to 10^{12} cm^{-3} would intensify interfacial recombination losses, thereby limiting charge extraction efficiency. These results highlight that the reported efficiencies represent upper performance limits, and achieving comparable performance experimentally requires careful control of material quality and interface engineering.

Although $Tl_2AgAsCl_6$ and Tl_2AgAsI_6 exhibit indirect band gap characteristics, as confirmed by the separation of the VBM and CBM in the calculated band structures, the implications of this indirect nature on photovoltaic performance require careful consideration. In indirect semiconductors, optical transitions near the band edge necessitate phonon-assisted momentum conservation, which generally leads to weaker absorption coefficients in the near-edge region compared to direct band gap materials. Consequently, such materials may exhibit reduced carrier generation for photons with energies close to the band gap and increased susceptibility to phonon-assisted recombination.

However, our DFT-calculated optical properties reveal that both compounds possess exceptionally high absorption coefficients on the order of ~10^5 cm^{-1} within the visible spectrum (6.07×10^5 cm^{-1} for $Tl_2AgAsCl_6$ and 6.05×10^5 cm^{-1} for Tl_2AgAsI_6). Although the fundamental transition is indirect, strong direct transitions occur at slightly higher photon energies, resulting in substantial optical absorption within the most intense region of the AM1.5 G solar spectrum. Since SCAPS-1D utilizes the calculated absorption coefficient $\alpha(\omega)$ to determine photogeneration rates, this strong visible absorption significantly supports the high simulated short-circuit current density. Furthermore, the electronic properties of these materials mitigate recombination-related limitations typically associated with indirect absorbers. The low electron effective masses (0.17 for $Tl_2AgAsCl_6$ and 0.09 for Tl_2AgAsI_6) and low exciton binding energies facilitate rapid exciton dissociation and efficient carrier transport. These properties enhance charge extraction before bulk recombination can dominate. Consistent with the behavior of successful indirect band gap absorbers such as crystalline silicon, absorber thickness optimization is crucial. Our simulation results demonstrate that increasing the absorber thickness significantly improves device efficiency, particularly for $Tl_2AgAsCl_6$, confirming the necessity of thicker active layers to effectively harvest long-wavelength photons. It should be emphasized that the reported power conversion efficiencies of 23.38% and 16.76% represent optimized theoretical limits under the controlled defect densities and ideal interface conditions assumed in SCAPS-1D. In practical devices, additional non-radiative recombination mechanisms, particularly trap-assisted recombination at grain boundaries and interfaces, may reduce performance. It is important to highlight that, in order to correctly interpret the simulated results, the power conversion efficiencies reported here (23.38% and 16.76%) are the maximum achievable under idealized SCAPS-1D conditions. Optimally aligned bands, bulk and interface total densities as low as 10^{10} cm^{-3} and ideality in charge transport across interfaces are assumed in the simulation, representing the upper theoretical limits of device performance. However, in potholes of real-world practices, many of non-ideal effects such as trap-assisted recombination, grain boundary defects, imperfect interface, also in limited material synthesis and layer deposition, could severely harm device performance. Moreover, non-uniformity in carrier density, dilution of mobility, and contact resistance during the fabrication track could also lower the PCE which is possible to achieve. Thus, the efficiencies reported are to be viewed as indicative of the hypothetical best potential of the systems proposed, and can be expected to represent lower limits for experimental devices. It is crucial to emphasize that the high-power PCE of 23.38% and 16.76% predicted by the SCAPS-1D simulations for $Tl_2AgAsCl_6$ and Tl_2AgAsI_6, respectively, must be interpreted as theoretical upper limits. These simulated values are derived from the materials' intrinsic optoelectronic capabilities such as their high optical absorption coefficients under idealized boundary conditions. The current model assumes optimal band alignment, perfect interfaces, and unrealistically low defect densities, which effectively eliminates the trap-assisted and interface recombination losses that typically plague experimental devices. Furthermore, while the exploration of these lead-free double halide perovskites is driven by the need to mitigate the toxicity and long-term instability of traditional lead-based variants, the practical realization of these devices will require overcoming significant material engineering hurdles. Future experimental work and more complex sensitivity analyses will be necessary to quantify the inevitable efficiency drops caused by deep-level defects, non-ideal charge transport layers, and operational degradation. Therefore, the device-level predictions presented here serve to establish the fundamental thermodynamic potential of the Tl_2AgAsX_6 family, providing a baseline target for future experimental optimization rather than an immediate projection of physical device performance.

3.7. Thermo-electric properties

In Thermoelectricity, the materials themselves are used for power generation, cooling, and temperature measurements, controlling electrical properties. Over the past century, more than 50% of metallic and

Table 6
Performance-based comparison of double perovskite absorbers.

Material	PCE (%)	Reference No.
$Cs_2AgBiBr_6$	25.92 (Theo.)	[78]
$Cs_2CuBiCl_6$	1.87 (exp)	[79]
Cs_2SnI_6	23.64 (Theo.)	[80]
Cs_2PdBr_6	24.19 (Theo.)	[81]
Cs_2PtI_6	26.50 (Theo.)	[82]
$Rb_2AuScBr_6$	27.49 (Theo.)	[83]
$Rb_2AuScCl_6$	22.41 (Theo.)	[83]
$Tl_2AgAsCl_6$	23.38 (Theo.)	This work
Tl_2AgAsI_6	16.76 (Theo.)	This work

semiconducting materials have been screened for their thermoelectric behavior. The thermoelectric properties of these materials are described by the transport coefficients such as electrical conductivity (σ), Seebeck coefficient (S), electronic thermal conductivity (K_e), power factor (PF), and dimensionless figure of merit (ZT). To understand the potential of Tl_2AgAsX_6 (X = Cl, I) for thermoelectric applications, these properties are investigated to estimate the charge carrier mobility, voltage per temperature gradient, and overall conversion efficiency [84].

The thermoelectric properties are calculated using the BoltzTraP2 code with a relaxation time (τ) taken as $10^{-14}s$ [44]. Although this simplifying assumption allows for a theoretical model, it may be an incomplete description of thermally responsive scattering mechanisms in actual materials. The calculated transport parameters such as the σ,S, K_e, and PF are estimated in the temperature range between 100 and 1000 K, and the corresponding temperature dependence of the parameters is depicted in Fig. 11(a-e) & Fig. 12(a-c). Electrical conductance symbolizes the capacity for an object to transport an electric current, which enhances with temperature since the carriers are thermally excited across the band gap of a semiconductor. The scaling of the conductivity with $\sigma = Ne\mu$, where is the mobility, indicates that, as more carriers are added, the conductance is increased [85]. This increment may increase K_e, following the Wiedemann–Franz Law, $K_e = L\varphi T$, where L indicates Lorentz number and T indicates absolute temperature [86]. The increasing trend with the temperature for σ and K_e, typical of semiconductors, is due to an increased carrier excitation to reach the equilibrium with the thermal. Nevertheless, it is important to optimize

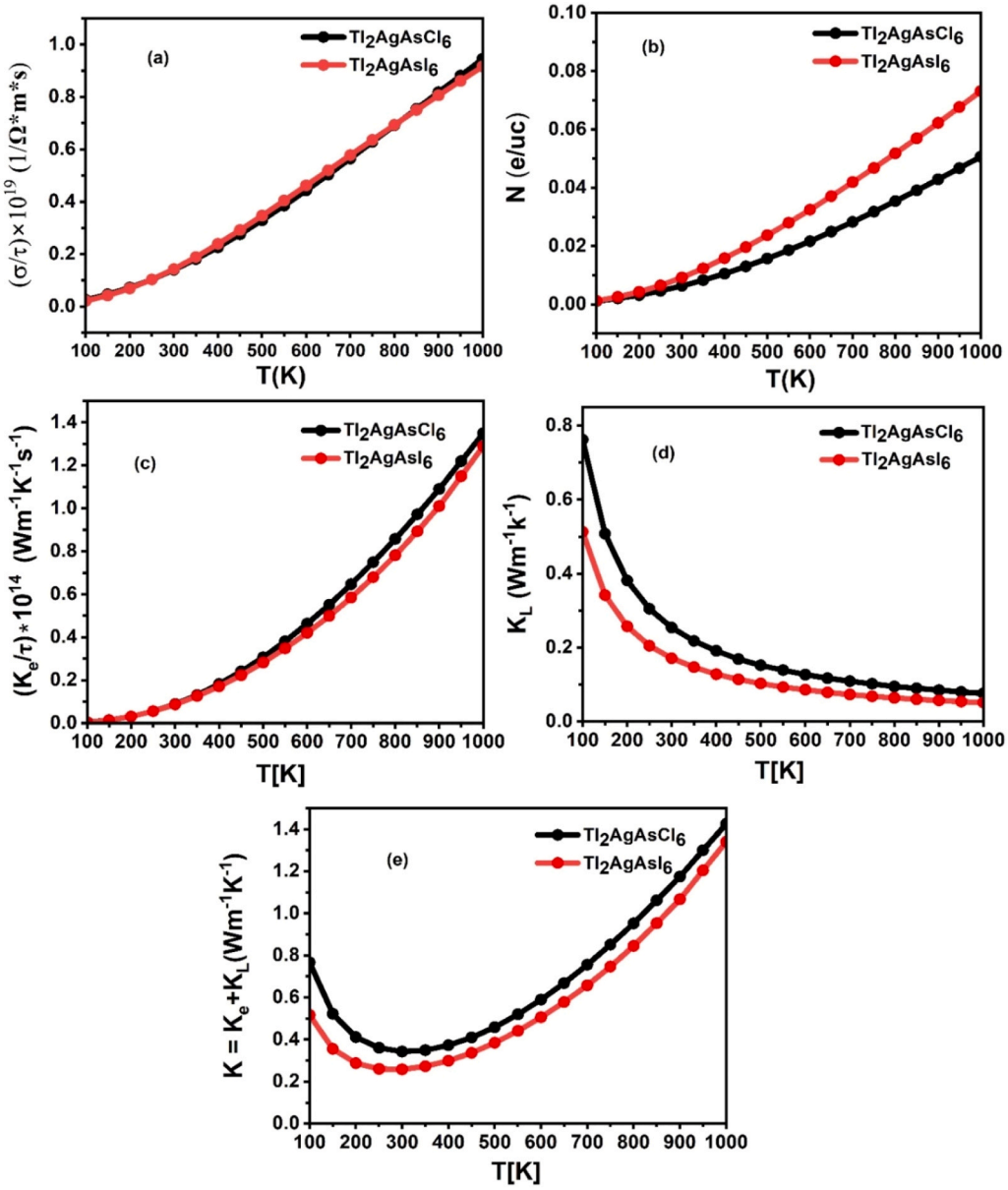

Fig. 11. (a) σ/τ (Electrical conductivity), (b) N (Carrier concentration), (c) K_e (Electronic conductivity), (d) K_L (Lattice conductivity), and (e) K (Total conductivity).

these parameters to enhance the *ZT*. As is seen in Fig. 11(a) and Fig. 11 (b), while keeping the temperature gradient (σ and N) required for the thermoelectric process. Additional reduction of K_L without sacrificing high σ by way of approaches like doping or nano structuring can further improve *ZT* and make Tl_2AgAsX_6 more applicable for potential utilization. Thermal conductivity portrays the competence of the material to demeanor heat, which involves K_L conducted by lattice vibration and K_e due to charge carrier movement [87]. For K_e increases with the temperature, as a result of increased electron excitation and enhancement of charge carrier mobility. In the room temperature (300 K), K_e values for $Tl_2AgAsCl_6$ and Tl_2AgAsI_6 are 0.089 and 0.0873 displayed in Fig. 11(c). On the other hand, the K_L obtained from the Slack equation decreases with an increase in temperature, as presented in Fig. 11(d), which is consistent with suppressed phonon-mediated heat transfer [88]. At room temperature, K_L values of $Tl_2AgAsCl_6$ and Tl_2AgAsI_6 are 0.254 and 0.171 $Wm^{-1}K^{-1}$, respectively. The total thermal conductance $K_{total} = K_L + K_e$, constituted in Fig. 11(e), balances these contributions [89]. A low K_{total} (0.26) primarily due to the reduced K_L, effectively minimizes heat loss and helps retain the temperature gradient in thermoelectric devices. The Seebeck coefficient (S) indicates the dominant carrier type and the ability of a material to convert heat into electrical energy [90]. A positive *S* means that the p-type conduction dominates and the holes are the major carriers. In Fig. 12(a) *S* values at 300 K of $Tl_2AgAsCl_6$ and Tl_2AgAsI_6 are 257 μVK^{-1} and 268 μVK^{-1}. The electronic band dispersion in the vicinity of the Fermi level influences both *S* and σ inversely. For the calculation of *S* we have [91]:

$$S = \left(\frac{8\pi^2 K_B^2}{3h^2 e}\right)\left(\frac{\pi}{3N}\right)^{\left(\frac{2}{3}\right)} m^* T \tag{23}$$

where m^* effective mass, high band dispersion near the Fermi level leads to a reduced m^* value, improving the carrier mobility as well as the *S*. Values of *S* above 268 μVK^{-1} suggest a high potential for thermoelectric power generation [92]. Favorable band dispersion facilitates high *S*, rendering them suitable for converting waste heat into useful electricity under significant temperature gradients. The $PF = S^2\sigma$ indicates a conversion efficiency of thermal energy to electrical energy of a material through a combination of the *S* and σ[93]. For Tl_2AgAsX_6 (X = Cl, I), PF increases with increasing temperature, as shown in Fig. 12(**b**) , $1.49 \times 10^{-04} - 5.06 \times 10^{-04} Wm^{-1}K^{-2}$ for $Tl_2AgAsCl_6$ and $1.41 \times 10^{-04} - 4.42 \times 10^{-04} Wm^{-1}K^{-2}$ for Tl_2AgAsI_6, between 100 and 1000 K. This increase originates from an optimal doping level that balances *S* and σ effectively, which optimizes the thermoelectric performance for higher temperatures. The performance of a thermoelectric material is evaluated using the figure of merit (*ZT*), in which T is temperature in K [94].

$$ZT = \frac{S^2\sigma}{(K_e + K_L)} \tag{24}$$

The Temperature dependence of *ZT* is plotted in Fig. 12(c), indicates its strong dependence on temperature, namely the increase of *ZT* with rising temperature, which is typical behavior for semiconductors. a typical behavior for semiconductors. The maximum value of $Tl_2AgAsCl_6$ and Tl_2AgAsI_6 between 500 and 550 K are 0.48 and 0.58. However, the values decrease between 600 and 1000 K, indicating these double-halide perovskites may be used in industrial heat management. Their modest optimal performance and stability up to 500 K render them promising candidates for application in the automobile exhaust recovery or industrial furnace environment where efficient energy conversion is crucial. Thermoelectric properties such as the *S*, σ, and K_e are then calculated with the BoltzTraP2 tool as a function Temperature based on the structural and electronic properties for Tl_2AgAsX_6. These changes in parameters are illustrated in Figs. 11 and 12. The BoltzTraP2 code was used to calculate the thermoelectric transport coefficients under constant relaxation time approximation (CRTA). A constant relaxation time of the order of $\sim 10^{-14}$ s is typically assumed in CRTA-based BoltzTraP2 calculations. This method assumes a constant carrier relaxation time and

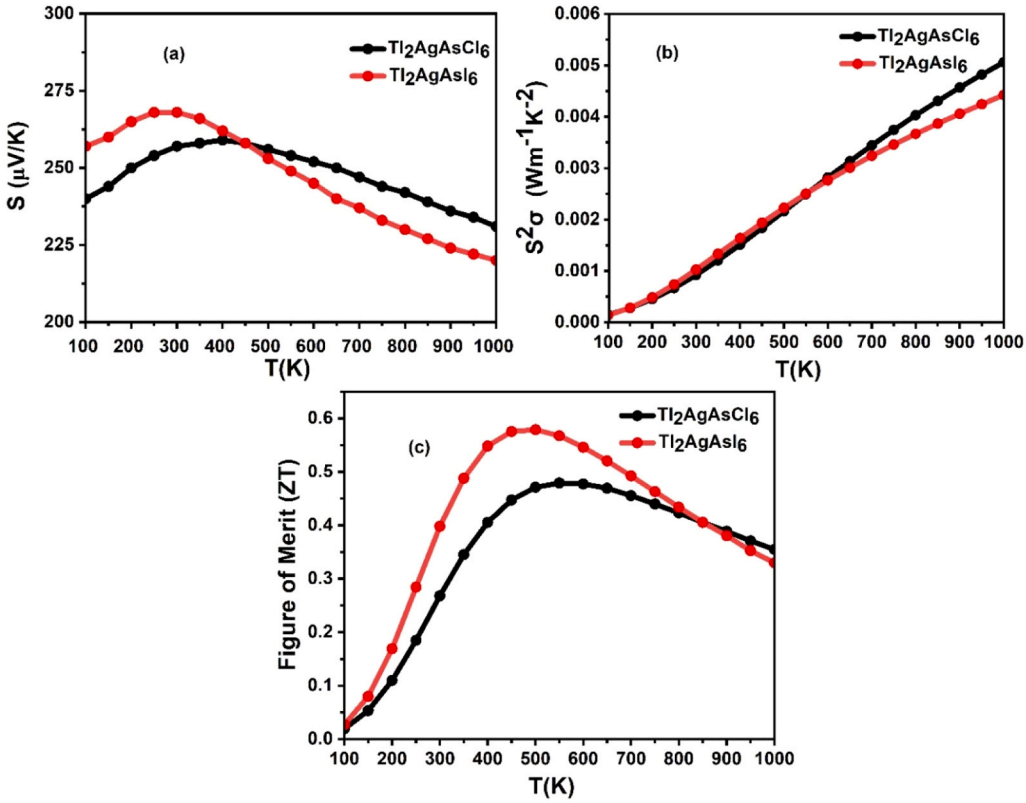

Fig. 12. (a) *S* (Seebeck coefficient), (b) $S^2\sigma$ (Power factor), and (c) *ZT* (Figure of merit).

Table 7
Calculated thermoelectric properties of studied materials.

Compound	$(\sigma/\tau) \times 10^{19}$ (1/ Ωms)	$(K_e/\tau) \times 10^{14}$ (W/ m*K*s)	S (μVK^{-1})	$PF \times 10^4$ (W/mk^2)	ZT (Maximum)
$Tl_2AgAsCl_6$	0.385	0.381	254	2.49	0.48
Tl_2AgAsI_6	0.347	0.282	253	2.23	0.58

ignores scattering processes (e.g., electron–phonon coupling) and its temperature dependence explicitly. As such, the calculated transport coefficients and figure of merit (ZT) are only to be taken as qualitative guides to transport behavior, not as quantitative predictions of reliability. Especially the absolute values of ZT are not suited for direct comparison with experimental data. Though analogous CRTA-based methodologies have been utilized in a number of earlier first-principles studies of perovskite materials, such treatment should be considered a lower-bound estimate compared to a rigorous solution based on explicit consideration of scattering processes and temperature-dependent relaxation times [95,96].

4. Conclusion

DFT has been utilized in this study to investigate the photovoltaic and thermoelectric energy harvesting applications of the optimized structure of the double perovskites under investigation. The analysis using tolerance factors and octahedral shows values in the ranges of 0.90–0.93 and 0.40–0.48, respectively. The mechanical characteristics confirm ductility, with B/G ratios greater than 1.75 and Poisson's ratios exceeding 0.26, both above their critical limits. The indirect band gaps of the Cl- and I-based halides were determined to be 1.692 eV and 0.811 eV, with transitions presented along the L–X symmetry path. Contributions to the conduction band minimum (CBM) are mainly from As-d, Ag-s, and X-p orbitals, whereas the valence band maximum (VBM) is dominated by Ag-d orbitals. This electronic configuration results in low effective carrier masses and a favorable density of states, making these materials promising for clean-energy technologies.

A negative dielectric constant was observed in the ultraviolet region, indicating potential applications in optical systems such as filters, fiber-optic components, and electromagnetic shielding. Refractive index at zero-energy was estimated to be 2.17 for Cl and 2.78 for I. $Tl_2AgAsCl_6$ and Tl_2AgAsI_6 have a high absorption coefficient in the visible spectrum, 6.07×10^5 cm^{-1} and 6.05×10^5 cm^{-1}, along with photovoltaic efficiency 23.38% and 16.76%, making them promising for optoelectronic devices. Both compounds exhibit p-type semiconducting behavior, confirmed by their positive Seebeck coefficients. It is particularly worth mentioning that the ZT values of the I-based compound are superior to those of the Cl-based system, reaching 0.40 and 0.27 at 300 K, respectively. This demonstrates that the narrower band gap of the I-based perovskite not only enhances solar absorption but also promotes efficient conversion of waste heat into electricity. The significance of halide double perovskites therefore, extends beyond optoelectronic to thermoelectric application. Although the optoelectronic properties are promising, the toxicity of thallium compromises the device application of Tl-based compounds. Any such device implementation would entail extreme encapsulation, fabrication method control, and environmental process safety issues. So these materials must be considered first and foremost models for high-performing photophysical behavior rather than immediate movers into renewable energy technologies.

CRediT authorship contribution statement

R.M. Tanvir: Writing – original draft, Methodology, Formal analysis, Data calculations, Validation. **Md. Al-Amin:** Writing – review & editing, Investigation, Validation. **S. Sheikh:** Writing – review & editing, Investigation, Validation. **A. Rayhan:** Writing – review & editing, Validation. **S. Mahmud:** Conceptualization, Formal analysis, Methodology, Validation, Writing – review & editing, Supervision, Project administration.

Declaration of Competing Interest

The authors declare that they have no known competing financial interests or personal relationships that could have appeared to influence the work reported in this paper.

Acknowledgement

The authors gratefully acknowledge the Smart Computing Research Laboratory (SCRL), Department of Electrical and Electronic Engineering, Jatiya Kabi Kazi Nazrul Islam University (JKKNIU), Mymensingh-2224, Bangladesh, for providing the computational facilities and support essential to the completion of this work.

Data Availability

The datasets used and/or analysed during the current study available from the corresponding author on reasonable request.

References

[1] O.B. Awodumi, A.O. Adewuyi, The role of non-renewable energy consumption in economic growth and carbon emission: evidence from oil producing economies in Africa, Energy Strategy Rev. 27 (2020) 100434, https://doi.org/10.1016/j.ESR.2019.100434.
[2] M.M. Asghar, Z. Wang, B. Wang, S.A.H. Zaidi, Nonrenewable energy—environmental and health effects on human capital: empirical evidence from Pakistan, Environ. Sci. Pollut. Res. 27 (3) (2020) 2630–2646, https://doi.org/10.1007/S11356-019-06686-7.
[3] M. Dada, L. Zulberti, P. Nannipieri, L. Fanucci, S. Moranti, Inference and evaluation of deep convolutional neural networks on microchip's hardware accelerator vectorBlox, Proc. 2023 Eur. Data Handl. Data Process. Conf. Space EDHPC 2023 (2023), https://doi.org/10.23919/EDHPC59100.2023.10396304.
[4] I. Kougias, et al., Analysis of emerging technologies in the hydropower sector, Renew. Sustain. Energy Rev. 113 (2019) 109257, https://doi.org/10.1016/J.RSER.2019.109257.
[5] A. Kumar, S. Kumar, Solar flare effects on D-region ionosphere using VLF measurements during low- and high-solar activity phases of solar cycle 24, Earth Planets Space 70 (1) (2018), https://doi.org/10.1186/S40623-018-0794-8.
[6] Z. Deng, F. Wei, S. Sun, G. Kieslich, A.K. Cheetham, P.D. Bristowe, Exploring the properties of lead-free hybrid double perovskites using a combined computational-experimental approach, J. Mater. Chem. A Mater. 4 (31) (2016) 12025–12029, https://doi.org/10.1039/C6TA05817E.
[7] J. Haruyama, K. Sodeyama, L. Han, Y. Tateyama, First-principles study of ion diffusion in perovskite solar cell sensitizers, J. Am. Chem. Soc. 137 (32) (2015) 10048–10051, https://doi.org/10.1021/JACS.5B03615.
[8] H.J. Snaith, Perovskites: the emergence of a new era for low-cost, high-efficiency solar cells, J. Phys. Chem. Lett. 4 (21) (2013) 3623–3630, https://doi.org/10.1021/JZ4020162.
[9] S.A. Dar, B. Want, Direct band gap double perovskite halide $Cs_2ScInCl_6$ for optoelectronic applications—a first principle study, Comput. Condens. Matter 33 (2022) e00736, https://doi.org/10.1016/J.COCOM.2022.E00736.
[10] G. King, P.M. Woodward, Cation ordering in perovskites, J. Mater. Chem. 20 (28) (2010) 5785–5796, https://doi.org/10.1039/B926757C.
[11] Q. Chen, et al., Under the spotlight: the organic–inorganic hybrid halide perovskite for optoelectronic applications, Nano Today 10 (3) (2015) 355–396, https://doi.org/10.1016/J.NANTOD.2015.04.009.
[12] G. Volonakis, et al., Lead-free halide double perovskites via heterovalent substitution of noble metals, J. Phys. Chem. Lett. 7 (7) (2016) 1254–1259, https://doi.org/10.1021/ACS.JPCLETT.6B00376.
[13] A.H. Slavney, T. Hu, A.M. Lindenberg, H.I. Karunadasa, A bismuth-halide double perovskite with long carrier recombination lifetime for photovoltaic applications, J. Am. Chem. Soc. 138 (7) (2016) 2138–2141, https://doi.org/10.1021/JACS.5B13294.
[14] E.T. McClure, M.R. Ball, W. Windl, P.M. Woodward, Cs_2AgBiX_6 (X = Br, Cl): new visible light absorbing, lead-free halide perovskite semiconductors, Chem. Mater. 28 (5) (2016) 1348–1354, https://doi.org/10.1021/ACS.CHEMMATER.5B04231.

[15] A. Bibi, et al., Lead-free halide double perovskites: toward stable and sustainable optoelectronic devices, Mater. Today 49 (2021) 123–144, https://doi.org/10.1016/J.MATTOD.2020.11.026.

[16] L. Chu, et al., Lead-free halide double perovskite materials: a new superstar toward green and stable optoelectronic applications, *2019 11:1*, Nano-Micro Lett. 11 (1) (2019) 1–18, https://doi.org/10.1007/S40820-019-0244-6.

[17] X. Xu, Y. Zhong, Z. Shao, Double perovskites in catalysis, electrocatalysis, and photo(electro)catalysis, Trends Chem. 1 (4) (2019) 410–424, https://doi.org/10.1016/J.TRECHM.2019.05.006.

[18] S. Khawar, et al., First-principles calculations to investigate structural, electronic, optical, and magnetic properties of a scintillating double perovskite halide ($Cs_2LiCeCl_6$), J. Mater. Res. Technol. 21 (2022) 4790–4798, https://doi.org/10.1016/J.JMRT.2022.11.088.

[19] A.J. Kale, R. Chaurasiya, A. Dixit, Lead-free $Cs_2BB'X_6$ (B: Ag/Au/Cu, B′: Bi/Sb/Tl, and X: Br/Cl/I) double perovskites and their potential in energy conversion applications, ACS Appl. Energy Mater. 5 (9) (2022) 10427–10445, https://doi.org/10.1021/ACSAEM.2C00672.

[20] M.A. Ali, R.A. Alshgari, A.A. Awadh Bahajjaj, M. Sillanpää, The study of new double perovskites K_2AgAsX_6 (X = Cl, Br) for energy-based applications, J. Taibah Univ. Sci. 17 (1) (2023) 2170680, https://doi.org/10.1080/16583655.2023.2170680.

[21] A. Ayyaz, et al., DFT aided comparative screening of mechanical, optoelectronic, and transport properties of double perovskites Cs_2ScAuX_6 (X = Cl, Br, and I) for green energy applications, Inorg. Chem. Commun. 165 (2024) 112527, https://doi.org/10.1016/J.INOCHE.2024.112527.

[22] S. Mahmud, M.A. Ali, M.M. Hossain, M.M. Uddin, DFT aided prediction of phase stability, optoelectronic and thermoelectric properties of A_2AuScX_6 (A= Cs, Rb; X= Cl, Br, I) double perovskites for energy harvesting technology, Vacuum 221 (2024) 112926, https://doi.org/10.1016/J.VACUUM.2023.112926.

[23] O.A. Lozhkina, et al., Microstructural analysis and optical properties of $Cs_2BiAgBr_6$ halide double perovskite single crystals, Chem. Phys. Lett. 694 (2017) 18–22, https://doi.org/10.1016/j.cplett.2018.01.031.

[24] G. Nazir, et al., Tuning of band gap by anions (Cl, Br, I) of double perovskites Rb_2AgAsX_6 (Cl, Br, I) for solar cells and thermoelectric applications, Phys. Scr. 98 (2) (2023) 025811, https://doi.org/10.1088/1402-4896/ACAEC1.

[25] F. Aslam, H. Ullah, M. Hassan, Theoretical investigation of Cs_2InBiX_6 (X = Cl, Br, I) double perovskite halides using first-principle calculations, Mater. Sci. Eng. B 274 (2021) 115456, https://doi.org/10.1016/J.MSEB.2021.115456.

[26] S. Iqbal, et al., Tuning the optoelectronic and thermoelectric characteristics of narrow bandgap Rb_2AlInX_6(X= Cl, Br, I) double perovskites: A DFT study, Mater. Sci. Semicond. Process 143 (2022) 106551, https://doi.org/10.1016/J.MSSP.2022.106551.

[27] S.F. Hoefler, G. Trimmel, T. Rath, Progress on lead-free metal halide perovskites for photovoltaic applications: a review, *2017 148:5*, Mon. F. üR. Chem. - Chem. Mon. 148 (5) (2017) 795–826, https://doi.org/10.1007/S00706-017-1933-9.

[28] S. Bimli, V. Manjunath, S.R. Mulani, A. Miglani, O.S. Game, R.S. Devan, Theoretical investigations of all inorganic Cs_2SnI_6 double perovskite solar cells for efficiency ~ 30, Sol. Energy 256 (2023) 76–87, https://doi.org/10.1016/J.SOLENER.2023.03.059.

[29] A. Natik, Y. Abid, R. Moubah, M. Abid, H. Lassri, Ab-initio investigation of the structural, electronic and optical properties of lead-free halide Cs_2TiI_6 double perovskites, Solid State Commun. 319 (2020) 114006, https://doi.org/10.1016/J.SSC.2020.114006.

[30] Z. Zhang, et al., Hydrogenated $Cs_2AgBiBr_6$ for significantly improved efficiency of lead-free inorganic double perovskite solar cell, *2022 13:1*, Nat. Commun. 13 (1) (2022) 1–12, https://doi.org/10.1038/s41467-022-31016-w.

[31] B. Lee, et al., Air-stable molecular semiconducting iodosalts for solar cell applications: Cs_2SnI_6 as a hole conductor, J. Am. Chem. Soc. 136 (43) (2014) 15379–15385, https://doi.org/10.1021/JA508464W.

[32] G. García-Espejo, D. Rodríguez-Padrón, R. Luque, L. Camacho, G. De Miguel, Mechanochemical synthesis of three double perovskites: $Cs_2AgBiBr_6$, $(CH_3NH_3)_2TlBiBr_6$ and $Cs_2AgSbBr_6$, Nanoscale 11 (35) (2019) 16650–16657, https://doi.org/10.1039/C9NR06092H.

[33] A. Bhorde, et al., Structural, electronic, and optical properties of lead-free halide double perovskite Rb_2AgBiI_6: a combined experimental and density functional theory study, ES Mater. Manuf. 12 (2021) 43–52, https://doi.org/10.30919/esmm5f1042.

[34] G.M. Mustafa, A. Slam, S. Saba, N.A. Noor, M. Waqas Iqbal, A. Dahshan, Optoelectronic and thermoelectric characteristics of halide based double perovskites K_2YAgX_6 (X = Br, I) for energy storage applications, Polyhedron 229 (2023) 116184, https://doi.org/10.1016/J.POLY.2022.116184.

[35] S. Walia, et al., Transition metal oxides – thermoelectric properties, Prog. Mater. Sci. 58 (8) (2013) 1443–1489, https://doi.org/10.1016/J.PMATSCI.2013.06.003.

[36] M.Y. Sofi, M.S. Khan, M.A. Khan, Control of spin on ferromagnetism and thermoelectric properties of K_2GeMnX_6 (X = Cl, Br, I) halide perovskites: emerging candidates for semiconductor spintronics and thermoelectric applications, Mater. Adv. 5 (11) (2024) 4913–4931, https://doi.org/10.1039/D3MA01160G.

[37] M.Y. Sofi, M.S. Khan, M.A. Khan, Semiconducting ferromagnetism and thermoelectric performance of Rb_2GeMI_6 (M = V, Ni, Mn): a computational perspective, Mater. Adv. 6 (6) (2025) 2071–2089, https://doi.org/10.1039/D4MA01091D.

[38] M.Y. Sofi, M.S. Khan, M.A. Khan, Harnessing the half-metallicity and thermoelectric insights in Cs_2AgMBr_6 (M = V, Mn, Ni) double halide perovskites: a DFT study, Mater. Sci. Semicond. Process 186 (2025) 109023, https://doi.org/10.1016/J.MSSP.2024.109023.

[39] M.Y. Sofi, et al., Pioneering computational insights into the structural, magnetic, and thermoelectric properties of A_3XN (A=Co, Fe; X=Cu, Zn) anti-perovskites for advanced material applications, Mater. Sci. Semicond. Process 185 (2025) 108925, https://doi.org/10.1016/J.MSSP.2024.108925.

[40] K. Schwarz, DFT calculations of solids with LAPW and WIEN2k, J. Solid State Chem. 176 (2) (2003) 319–328, https://doi.org/10.1016/S0022-4596(03)00213-5.

[41] J.P. Perdew, K. Burke, M. Ernzerhof, Generalized gradient approximation made simple, Phys. Rev. Lett. 77 (18) (1996) 3865, https://doi.org/10.1103/PhysRevLett.77.3865.

[42] M. Jamal, M. Bilal, I. Ahmad, S. Jalali-Asadabadi, IRelast package, J. Alloy. Compd. 735 (2018) 569–579, https://doi.org/10.1016/J.JALLCOM.2017.10.139.

[43] K. Nakano, T. Sakai, Assessing the performance of the Tran-Blaha modified Becke-Johnson exchange potential for optical constants of semiconductors in the ultraviolet-visible light region, J. Appl. Phys. 123 (1) (2018), https://doi.org/10.1063/1.5006170/154610.

[44] G.K.H. Madsen, J. Carrete, M.J. Verstraete, BoltzTraP2, a program for interpolating band structures and calculating semi-classical transport coefficients, Comput. Phys. Commun. 231 (2018) 140–145, https://doi.org/10.1016/J.CPC.2018.05.010.

[45] W. Travis, E.N.K. Glover, H. Bronstein, D.O. Scanlon, R.G. Palgrave, On the application of the tolerance factor to inorganic and hybrid halide perovskites: a revised system, Chem. Sci. 7 (7) (2016) 4548–4556, https://doi.org/10.1039/C5SC04845A.

[46] Y. Fu, et al., Incorporating large a cations into lead iodide perovskite cages: relaxed goldschmidt tolerance factor and impact on exciton-phonon interaction, ACS Cent. Sci. 5 (8) (2019) 1377–1386, https://doi.org/10.1021/ACSCENTSCI.9B00367.

[47] A.E. Fedorovskiy, N.A. Drigo, M.K. Nazeeruddin, The role of Goldschmidt's tolerance factor in the formation of A_2BX_6 double halide perovskites and its optimal range, Small Methods 4 (5) (2020) 1900426, https://doi.org/10.1002/SMTD.201900426.

[48] C. Li, X. Lu, W. Ding, L. Feng, Y. Gao, Z. Guo, Formability of ABX3 (X = F, Cl, Br, I) halide perovskites, urn:issn:0108-7681 64 (6) (Nov. 2008) 702–707, doi:10.1107/S0108768108032734.

[49] N.H. Alotaibi, et al., DFT study of double perovskites Cs_2AgBiX_6 (X = Cl, Br): an alternative of hybrid perovskites, J. Solid State Chem. 313 (2022) 123353, https://doi.org/10.1016/J.JSSC.2022.123353.

[50] S. Kirklin, et al., The open quantum materials database (OQMD): assessing the accuracy of DFT formation energies, *2015 1:1*, npj Comput. Mater. 1 (1) (2015) 15010, https://doi.org/10.1038/npjcompumats.2015.10.

[51] E. Schreiber, O.L. Anderson, N. Soga, J.F. Bell, Elastic constants and their measurement, J. Appl. Mech. 42 (3) (1975) 747–748, https://doi.org/10.1115/1.3423687.

[52] M. Born, On the stability of crystal lattices. I, Math. Proc. Camb. Philos. Soc. 36 (2) (1940) 160–172, https://doi.org/10.1017/S0305004100017138.

[53] M.S. Parves, S. Mahmud, M. Tarekuzzaman, M.A. Rayhan, M. Rasheduzzaman, M. Z. Hasan, Structural and optoelectronic study of $MgLiX_3$ (X= Cl, Br, and I) halide perovskites: A DFT approach, AIP Adv. 14 (10) (2024), https://doi.org/10.1063/5.0231837/3318203.

[54] J. Wang, S. Yip, S.R. Phillpot, D. Wolf, Crystal instabilities at finite strain, Phys. Rev. Lett. 71 (25) (1993) 4182, https://doi.org/10.1103/PhysRevLett.71.4182.

[55] D.G. Pettifor, Theoretical predictions of structure and related properties of intermetallics, Mater. Sci. Technol. (United Kingdom) 8 (4) (1992) 345–349, https://doi.org/10.1179/MST.1992.8.4.345.

[56] R.M. Tanvir, S. Tanvir, M. Al-Amin, A. Rayhan, S. Mahmud, Computational analysis of hydrogen storage and physical behavior of Al, Ga, and In-based copper hydrides, Comput. Condens. Matter 45 (2025) e01175, https://doi.org/10.1016/J.COCOM.2025.E01175.

[57] X. Luan, H. Qin, F. Liu, Z. Dai, Y. Yi, Q. Li, The mechanical properties and elastic anisotropies of cubic Ni_3Al from first principles calculations, *2018, Vol. 8, Page 307*, Crystals 8 (8) (2018) 307.

[58] M.E. Fine, L.D. Brown, H.L. Marcus, Elastic constants versus melting temperature in metals, Scr. Metall. 18 (9) (1984) 951–956, https://doi.org/10.1016/0036-9748(84)90267-9.

[59] G. Murtaza, et al., Lead Free Double Perovsites Halides $X_2AgTlCl_6$ (X = Rb, Cs) for solar cells and renewable energy applications, J. Solid State Chem. 297 (2021) 121988, https://doi.org/10.1016/J.JSSC.2021.121988.

[60] T.M. Bhat, D.C. Gupta, Magneto-electronic, thermal, and thermoelectric properties of some Co-based quaternary alloys, J. Phys. Chem. Solids 112 (2018) 190–199, https://doi.org/10.1016/J.JPCS.2017.09.023.

[61] M. Markov, et al., Semi-metals as potential thermoelectric materials, Sci. Rep. 8 (1) (2018), https://doi.org/10.1038/S41598-018-28043-3.

[62] F. Tran, P. Blaha, Accurate band gaps of semiconductors and insulators with a semilocal exchange-correlation potential, Phys. Rev. Lett. 102 (22) (2009) 226401, https://doi.org/10.1103/PHYSREVLETT.102.226401.

[63] S. Mahmud, M.M. Hossain, M.M. Uddin, M.A. Ali, Prediction of X_2AuYZ_6 (X = Cs, Rb; Z = Cl, Br, I) double halide perovskites for photovoltaic and wasted heat management device applications, J. Phys. Chem. Solids 196 (2025) 112298, https://doi.org/10.1016/J.JPCS.2024.112298.

[64] G. Volonakis, et al., Lead-free halide double perovskites via heterovalent substitution of noble metals, J. Phys. Chem. Lett. 7 (7) (2016) 1254–1259, https://doi.org/10.1021/acs.jpclett.6b00376.

[65] G. Giorgi, J.I. Fujisawa, H. Segawa, K. Yamashita, Small photocarrier effective masses featuring ambipolar transport in methylammonium lead iodide perovskite: a density functional analysis, J. Phys. Chem. Lett. 4 (24) (2013) 4213–4216, https://doi.org/10.1021/JZ4023865.

[66] M.Y. Sofi, M.S. Khan, M.A. Khan, Eco-friendly lead-free halide double perovskites A_2CuMCl_6 (A = K, Rb; M = Sb, Bi): stability, thermoelectric, and optoelectronic advancements through theoretical insights, J. Mater. Chem. C Mater. 12 (39) (2024) 16045–16058, https://doi.org/10.1039/D4TC00891J.

[67] S. Mahmud, U. Ahmed, M.A.U.Z. Atik, M.M. Hossain, M.M. Uddin, M.A. Ali, Novel $Cs_2Au^{I}M^{III}F_6$ (M = As, Sb) double halide perovskites: sunlight and industrial waste heat management device applications, Phys. Chem. Chem. Phys. 27 (9) (2025) 4686–4703, https://doi.org/10.1039/D4CP04293J.

[68] C. Ambrosch-Draxl, J.O. Sofo, Linear optical properties of solids within the full-potential linearized augmented planewave method, Comput. Phys. Commun. 175 (1) (2006) 1–14, https://doi.org/10.1016/J.CPC.2006.03.005.

[69] D.R. Penn, Wave-number-dependent dielectric function of semiconductors, Phys. Rev. 128 (5) (1962) 2093, https://doi.org/10.1103/PhysRev.128.2093.

[70] S. Mahmud, M.A.U.Z. Atik, M.N. Mostakim, M. Tarekuzzaman, M.Z. Hasan, Investigation of direct small bandgap Cs_2AuInX_6 (X= F/Cl) double perovskites for energy harvesting technology employing DFT, Comput. Condens. Matter 40 (2024) e00950, https://doi.org/10.1016/J.COCOM.2024.E00950.

[71] G.M. Mustafa, et al., First principles study of double perovskites Li_2AgAsX_6 (X = Cl, Br, I) for optoelectronic and thermoelectric applications, RSC Adv. 15 (7) (2025) 5202–5213, https://doi.org/10.1039/D4RA07969H.

[72] J. Sun, H.T. Wang, J. He, Y. Tian, Ab initio investigations of optical properties of the high-pressure phases of ZnO, Phys. Rev. B Condens. Matter Mater. Phys. 71 (12) (2005) 125132, https://doi.org/10.1103/PHYSREVB.71.125132.

[73] P.R. Varadwaj, H.M. Marques, Physical and optoelectronic features of lead-free $A_2AgRhBr_6$ (A = Cs, Rb, K, Na, Li) with halide double perovskite composition, J. Mater. Chem. C. Mater. 8 (37) (2020) 12968–12983, https://doi.org/10.1039/D0TC02501A.

[74] A. Bafekry, et al., Semiconducting chalcogenide alloys based on the (Ge, Sn, Pb) (S, Se, Te) formula with outstanding properties: a first-principles calculation study, ACS Omega 6 (14) (2021) 9433–9441, https://doi.org/10.1021/ACSOMEGA.0C06024.

[75] H. Sabbah, Z. Abdel Baki, R. Mezher, J. Arayro, SCAPS-1D modeling of hydrogenated lead-free $Cs_2AgBiBr_6$ double perovskite solar cells with a remarkable efficiency of 26.3%, Nanomaterials 14 (1) (2023) 48, https://doi.org/10.3390/NANO14010048.

[76] M. Liu, M.B. Johnston, H.J. Snaith, Efficient planar heterojunction perovskite solar cells by vapour deposition, Nature 501 (7467) (2013) 395–398, https://doi.org/10.1038/NATURE12509.

[77] S.C. Baker-Finch, K.R. McIntosh, D. Yan, K.C. Fong, T.C. Kho, Near-infrared free carrier absorption in heavily doped silicon, J. Appl. Phys. 116 (6) (2014), https://doi.org/10.1063/1.4893176.

[78] A. Kumar, et al., Hydrogenated $Cs_2AgBiBr_6$ double perovskites: a sustainable lead-free route toward high-efficiency solar cells, Sci. Rep. 2026 (2026), https://doi.org/10.1038/S41598-026-47055-y.

[79] N. Neelu, N. Pandey, S. Chakrabarti, Synthesis, structural and optical properties of lead free $Cs_2CuBiCl_6$: a potential & promising eco-friendly double perovskite for solar cell applications, Opt. Mater. 143 (2023) 114250, https://doi.org/10.1016/J.OPTMAT.2023.114250.

[80] S. Porwal, M. Paul, H. Dixit, S. Mishra, T. Singh, Investigation of defects in Cs_2SnI_6-based double perovskite solar cells via SCAPS-1D, Adv. Theory Simul. 5 (9) (2022) 2200207, https://doi.org/10.1002/ADTS.202200207.

[81] T.M.U. Nisa, M. Kashif, R. Pandey, M. Malik, Design and optimization of novel double perovskite-Cs_2PdBr_6 solar cell with organic–inorganic charge transport layers: a numerical SCAPS-1D simulation, Phys. Scr. (2024), https://doi.org/10.1088/1402-4896/ADA475.

[82] M. Mehrabian, M. Taleb-Abbasi, O. Akhavan, Comparing the performances of Cs_2TiBr_6, $Cs_2AgBiBr_6$, and Cs_2PtI_6 halide compositions in double perovskite photovoltaic devices, *2025 14:2*, Mater. Renew. Sustain. Energy 14 (2) (2025) 38, https://doi.org/10.1007/S40243-025-00311-Z.

[83] M. Al-Amin, A. Haque, S. Mahmud, M.M. Hossain, M.M. Uddin, M.A. Ali, Numerical optimization of $Rb_2AuScBr_6$ and $Rb_2AuScCl_6$ -based lead-free perovskite solar cells: device engineering and performance mapping, RSC Adv. 15 (53) (2025) 45309–45330, https://doi.org/10.1039/D5RA07344H.

[84] J. Scheidemantel, C. Ambrosch-Draxl, T. Thonhauser, V. Badding, O. Sofo, Transport coefficients from first-principles calculations, Phys. Rev. B 68 (12) (2003) 125210, https://doi.org/10.1103/PhysRevB.68.125210.

[85] K. Kaur, R. Kumar, Effect of pressure on electronic and thermoelectric properties of magnesium silicide: a density functional theory study, Chin. Phys. B 25 (5) (2016) 056401, https://doi.org/10.1088/1674-1056/25/5/056401.

[86] W. Kim, Strategies for engineering phonon transport in thermoelectrics, J. Mater. Chem. C. Mater. 3 (40) (2015) 10336–10348, https://doi.org/10.1039/C5TC01670C.

[87] J.P. Heremans, et al., Enhancement of thermoelectric efficiency in PbTe by distortion of the electronic density of states, Science (1979) 321 (5888) (2008) 554–557, https://doi.org/10.1126/science.1159725.

[88] G.A. Slack, The thermal conductivity of nonmetallic crystals, Solid State Phys. - Adv. Res. Appl. 34 (C) (1979) 1–71, https://doi.org/10.1016/S0081-1947(08)60359-8.

[89] W. Li, et al., Crystal structure induced ultralow lattice thermal conductivity in thermoelectric Ag_9AlSe_6, Adv. Energy Mater. 8 (18) (2018), https://doi.org/10.1002/AENM.201800030.

[90] D. Narducci, E. Selezneva, G. Cerofolini, S. Frabboni, G. Ottaviani, Impact of energy filtering and carrier localization on the thermoelectric properties of granular semiconductors, J. Solid State Chem. 193 (2012) 19–25, https://doi.org/10.1016/J.JSSC.2012.03.032.

[91] X. Zhang, L.D. Zhao, Thermoelectric materials: energy conversion between heat and electricity, J. Mater. 1 (2) (2015) 92–105, https://doi.org/10.1016/J.JMAT.2015.01.001.

[92] K. Kutorasinski, B. Wiendlocha, S. Kaprzyk, J. Tobola, Electronic structure and thermoelectric properties of n - and p -type SnSe from first-principles calculations, Phys. Rev. B Condens. Matter Mater. Phys. 91 (20) (May 2015) 205201, https://doi.org/10.1103/PHYSREVB.91.205201.

[93] M.Y. Sofi, M.S. Khan, M.A. Khan, Control of spin on ferromagnetism and thermoelectric properties of K_2GeMnX_6 (X = Cl, Br, I) halide perovskites: emerging candidates for semiconductor spintronics and thermoelectric applications, Mater. Adv. 5 (11) (2024) 4913–4931, https://doi.org/10.1039/D3MA01160G.

[94] M.A. Ali, et al., Appealing perspectives of structural, electronic, mechanical, and thermoelectric properties of $Tl_2(Se,Te)Cl_6$ vacancy-ordered double perovskites, J. Phys. Chem. Solids 159 (2021) 110258, https://doi.org/10.1016/J.JPCS.2021.110258.

[95] M.Y. Sofi, M.S. Khan, M. Ajmal Khan, Spin exchange, electronic correlation, and thermoelectric transport in Rb_2GeMBr_6 (M = V, Mn, Ni) halide double perovskites from first principles calculations, J. Mater. Chem. C Mater. 14 (1) (2026) 444–467, https://doi.org/10.1039/D5TC01842K.

[96] M.Y. Sofi, D.C. Gupta, Scrutinized the inherent spin half-metallicity and thermoelectric response of f-electron-based $RbMO_3$ (M = Np, Pu) perovskites: a computational assessment, *2022 12:1*, Sci. Rep. 12 (1) (2022) 19476, https://doi.org/10.1038/s41598-022-22633-y.